MitoFit Preprint Arch (2019) doi:10.26124/mitofit:190003
Posted online 2019-06-11 Open Access

OXPHOS remodeling in high-grade prostate cancer involves mtDNA mutations and a prognostic gene expression signature

Bernd Schöpf[1], Hansi Weissensteiner[1], Georg Schäfer[2], Federica Fazzini[1], Pornpimol Charoentong[3], Andreas Naschberger[1], Bernhard Rupp[1], Liane Fendt[1], Valesca Bukur[4], Irina Eichelbrönner[4], Patrick Sorn[4], Ugur Sahin[4], Florian Kronenberg[1], Erich Gnaiger[5], Helmut Klocker[6*]

Author affiliations

[1]Division of Genetic Epidemiology, Department of Medical Genetics, Molecular and Clinical Pharmacology; Medical University of Innsbruck, Schöpfstrasse 41, A-6020 Innsbruck, Austria
[2]Department of Pathology, Medical University of Innsbruck, Müllerstraße 44, A-6020 Innsbruck, Austria
[3]Department of Medical Oncology, National Center for Tumor diseases, University Hospital Heidelberg, Im Neuenheimer Feld 267, D-69120 Heidelberg, Germany.
[4]TRON, Translationale Onkologie an der Universitätsmedizin der Johannes-Gutenberg-Universität Mainz gGmbH, Freiligrathstraße 12, D-55131 Mainz, Germany
[5]Department of Visceral, Transplant and Thoracic Surgery, D. Swarovski Research Laboratory, Medical University of Innsbruck, Innrain 66/6, A-6020 Innsbruck, Austria
[6]Division of Experimental Urology, Department of Urology, Medical University of Innsbruck, Anichstraße 35, A-6020 Innsbruck, Austria

*To whom correspondence should be addressed:

Address for correspondence:
Helmut Klocker, PhD
Division of Experimental Urology, Department of Urology, Medical University Innsbruck
Anichstraße 35, A-6020 Innsbruck, Austria
Phone: +43 50 504 24818; E-Mail: helmut.klocker@i-med.ac.at

http://www.mitofit.org/index.php/Schoepf_2019_MitoFit_Preprint_Arch

Editor MitoFit Preprint Archives: Gnaiger E

Keywords:

Mitochondria, high-resolution respirometry, oxidative phosphorylation, mitochondrial DNA mutation, mtDNA heteroplasmy, metabolic reprograming

Running title: Mitochondrial metabolic remodeling in human prostate cancer tissue

Abstract

Rewiring of energy metabolism and adaptation of mitochondrial respiratory functions are considered to impact on prostate cancer development and progression. High-resolution respirometry of paired benign and malignant human prostate tissue samples revealed reduced respiratory capacities with NADH-pathway substrates glutamate and malate in malignant tissue and a significant metabolic shift towards respiratory capacity with succinate, particularly in high-grade tumors. The load of potentially deleterious mitochondrial-DNA mutations was higher in tumor tissue and associated with unfavorable risk factors. High levels of potentially deleterious mutations in mitochondrial Complex I-encoding genes were associated with a 70% reduction in NADH-pathway capacity and compensation by increased S-pathway capacity. Structural analyses of these mutations revealed amino acid alterations leading to potentially deleterious effects on Complex I, supporting a causal relationship. RNA-seq revealed a signature of metabolic enzymes corresponding to the altered mitochondrial respiratory pathways and enabled extraction of a metagene set for prediction of shorter disease-free survival.

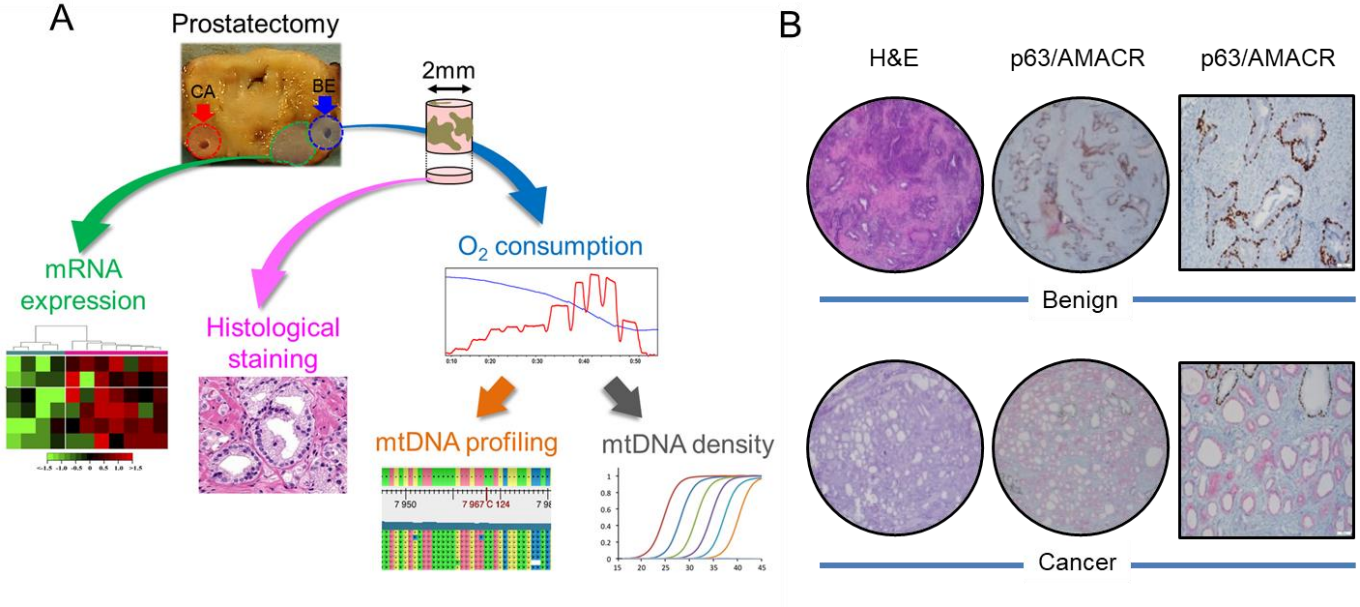

Fig. 1. Sample workflow and histological staining. A. From each of 50 radical prostatectomy specimens a tumor and a non-malignant benign tissue punch needle biopsy was extracted by an experienced uropathologist from contralateral sites of the specimens. While a small portion of the extracted tissue cores (blue area) was fixed and used for histological stainings (pink arrow) and confirmation of tissue identity, the rest was used immediately for high-resolution respirometry (HRR, blue arrow), subsequent NGS mtDNA profiling (orange arrow) and mtDNA copy number determination (grey arrow). From 16 cases of this cohort, frozen tissue samples directly adjacent to the biopsy cores (green area) were isolated by macrodissection followed by RNA extraction for gene expression profiling via total RNA-NGS (green arrow). **B.** Hematoxylin and eosin staining (H&E), p63 (non-malignant tissue marker, brown) and AMACR (malignant cell marker, red) double-immunostaining (p63/AMACR) of fixed and paraffin embedded benign and cancerous prostate tissue samples extracted for HRR.

Introduction

Prostate cancer (PCa) is the most prevalent male non-cutaneous cancer type in Western countries, accounting for an estimated 10% of all cancer related deaths in Europe (Malvezzi et al., 2015). While the exact molecular mechanisms of PCa initiation remain poorly understood, recent studies suggest a multifactorial etiology encompassing an accumulation of genetic and epigenetic aberrations leading to a stepwise dedifferentiation and uncontrolled

proliferation of the prostatic epithelium (Packer and Maitland, 2016). The genomic landscape of primary PCa has been extensively studied, but only few genomic aberrations including PTEN deletion, TMPRSS-ERG fusions and CDKN1B deletion but no driver mutations are commonly found in primary human disease (Berger et al., 2011). Among other carcinogenic alterations, adaptations in metabolism and energy turnover might contribute to PCa formation and progression.

Alterations in mitochondrial (mt) metabolism including oxidative phosphorylation (OXPHOS) are a hallmark of cancer (Pavlova and Thompson, 2016). Moreover, mitochondria play an important role during tumorigenesis by orchestrating cellular energy transformation, apoptosis and ROS signaling (Valcarcel-Jimenez et al., 2017). The bulk of cellular ATP is produced in the mitochondria by the stepwise oxidation of substrates via the tricarboxylic acid (TCA) cycle. Electrons are fueled into the mitochondrial electron transfer system (ETS), catalyzed by NADH and succinate-linked dehydrogenases in the mt-matrix and mt-inner membrane. Translocation of protons generates an electrochemical potential difference across the mt-inner membrane, which is used by ATP synthase to phosphorylate ADP to ATP. Only limited data on TCA cycle and OXPHOS activity in primary PCa tissue is available and little is known about the specific malignant PCa metabolism (Dueregger et al., 2015).

While the majority of ETS machinery proteins are encoded by nuclear DNA (nDNA), 13 essential ETS subunits are encoded by mtDNA, a small circular genome located in the mitochondrial matrix. mtDNA mutations have been linked to PCa formation and progression (Petros et al., 2005; Arnold et al., 2009). Compared to nDNA, mtDNA exhibits a higher mutation rate caused by an increased exposure to ETS derived reactive oxygen species (ROS) and a less efficient DNA repair system (Quinlan et al., 2012). Random segregation and subpopulation replication of mtDNA variants lead to the phenomenon of “heteroplasmy” (HP), the presence of different populations of mtDNA variants in a mitochondrion, cell or tissue (Wai et al., 2008). mtDNA single nucleotide variants are frequently found in localized prostate cancer (Hopkins et al., 2017), however, their functional consequences on mitochondrial metabolism remain elusive. Understanding the impact of mtDNA mutations might help to characterize metabolic adaptations exploited to drive PCa formation and progression. In this study, we aim to unravel the interplay between mtDNA mutations, the expression and function of mitochondrial enzymes and the metabolic PCa phenotype to identify specific mitochondrial biomarkers and therapeutic targets.

Results

Shift to succinate-driven OXPHOS in prostate tumors

Paired benign and malignant prostate tissue samples were isolated immediately after radical prostatectomy from fifty prostate cancer patients. Benign samples were taken distant from the tumor to minimize possible field effects, normally from the contralateral site (Fig. 1A). A small portion of each biopsy was used for diagnostic staining and validation of tissue identity (Fig. 1B) while the rest of the tissue was subjected to high-resolution respirometry (HRR). Patient characteristics, tumor features and gradings are depicted in Table 1. Mitochondrial metabolism and OXPHOS capacities in paired benign and malignant tissue biopsies of each prostate specimen were analyzed simultaneously by sequentially assessing respiratory capacities of single and combined mt electron transfer (ET) pathways using a previously published substrate-uncoupler-inhibitor-titration (SUIT) protocol with slight modifications (Schoepf et al. 2016, Figure 2A-C, Tables S1, S2). A short-term treatment with H2O2 was included to simulate oxidative stress.

Benign tissues showed a significantly higher NADH-pathway OXPHOS capacity (N; electron entry to the Q-junction via CI) supported by glutamate&malate, GM_P, and pyruvate&glutamate&malate, N $(PGM)_P$, respectively, compared to PCa tissue ($p = 1.6 \cdot 10^{-5}$ and $p = 8.3 \cdot 10^{-6}$, Fig. 2D). However, upon further addition of succinate (S), no differences in the OXPHOS (NS_P) and ET (NS_E) respiratory capacities were observed, indicating compensation of the N-pathway deficiency by increased convergent electron transfer through the succinate-pathway (electron entry to Q via CII). Full restoration of NS_P- and NS_E-capacities in tumor tissue was driven largely by succinate and to a smaller extent by pyruvate. Enabling of

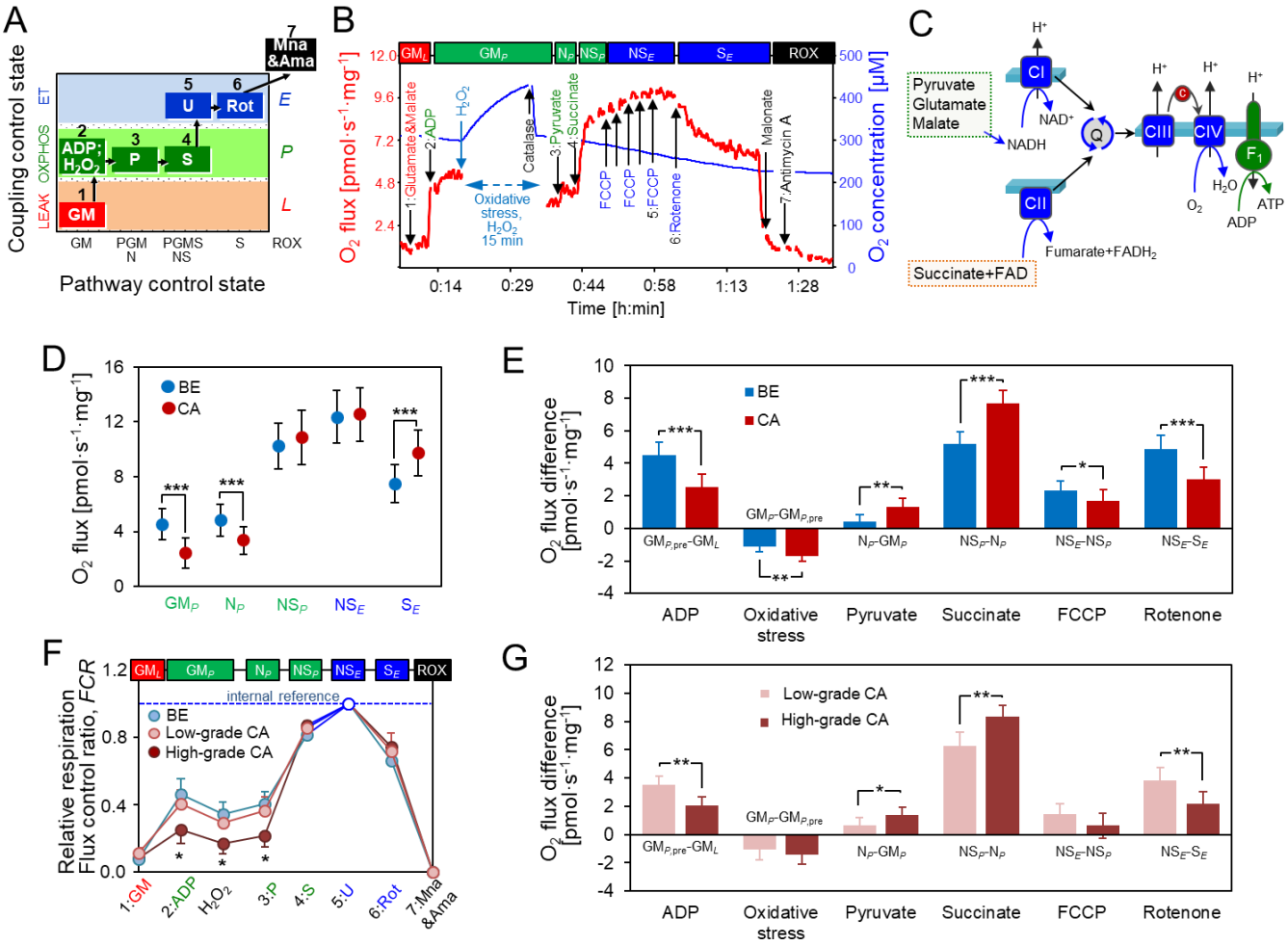

Fig. 2. High-resolution respirometry (HRR) of prostate tissue samples. A. Coupling/pathway control diagram showing the sequential steps in the substrate-uncoupler-inhibitor titration (SUIT) protocol with different coupling states (rates). Substrates: [1] Glutamate, G, and Malate, M, inducing the LEAK state (GM_L); [2] ADP, inducing the OXPHOS state (GM_P); subsequently oxidative stress by H_2O_2 for 15 min followed by H_2O_2 inactivation by catalase; [3] Pyruvate, P (PGM_P or N_P); [4] Succinate, S (NS_P). Uncoupler: [5] FCCP, U, inducing the ET state (NS_E). Inhibitors: [6] Rotenone, Rot (S_E); [7] Malonate, Mna, and Antimycin A, Ama, inducing the state of residual oxygen consumption, ROX (*Rox*). For details see Tables S1 and S2 and Gnaiger *et al.* (2019). **B.** Representative HRR traces with permeabilized tissue in the Oroboros O2k. Red line (left *Y* axis): wet mass-specific O_2 flux (oxygen consumption [pmol·s^{-1}·mg^{-1}]). Blue line (right *Y* axis): O_2 concentration [µM]. Substrate-uncoupler-inhibitor titrations are indicated by arrows. Different coupling/pathway control states are indicated in boxes: LEAK (red); OXPHOS (green); ET (blue); ROX (black). **C.** Schematic representation of mitochondrial electron transfer from NADH-linked substrates through Complexes CI, CIII and CIV (N-pathway) and from succinate through CII, CIII and CIV (S-pathway). Glutamate, malate and pyruvate support the N-pathway through CI into the Q-cycle (Q); succinate provides electrons via CII into Q. Electrons are transferred from CIII via cytochrome *c* (c) to CIV where O_2 is reduced to water. H^+ ions are pumped across the inner mitochondrial membrane by CI, CIII and CIV to generate an electrochemical potential difference across the mitochondrial inner membrane, which drives phosphorylation of ADP to ATP by F_OF_1-ATPase. **D.** Respiratory capacity in benign (blue) versus malignant (red) tissue: OXPHOS-capacity (GM_P, N_P and NS_P) and ET-capacity (NS_E). **E.** Effects of substrates glutamate&malate, pyruvate, succinate, oxidative stress, uncoupler FCCP, and CI inhibitor rotenone on O_2-flux in benign (blue) and malignant (red) tissue samples. **F.** Normalized respiratory capacities of high-grade tumor (Gleason>7; red; *N*=10) and low-grade tumor (Gleason ≤7, light-red, *N*=40) samples compared to benign samples (blue). **G.** Effects of

substrates, oxidative stress, uncoupler, and CI inhibitor on O_2-flux in low-grade (light red) and high-grade (red) tissue samples.

glutamate&malate-driven OXPHOS by addition of ADP triggered an increase of O_2-flux of 2.4 pmol s^{-1} mg^{-1} in tumor compared to 4.5 pmol s^{-1} mg^{-1} in benign tissue samples (Fig. 2E). Addition of pyruvate and succinate, respectively, elicited significantly higher increases of O_2-flux in malignant compared to benign samples (N_P-GM_P, and NS_P-N_P) and thus recovered full respiratory capacity in tumors (Fig. 2E). Finally, CI inhibition with rotenone confirmed significantly higher NADH pathway capacity of benign compared to tumor tissue (NS_E-S_E, Fig. 2E). Oxidative stress resulted in a reduction of O_2-flux in both tissue types, however, significantly more in the tumor tissue (1.7 vs. 1.1 pmol s^{-1} mg^{-1}, p=4.2·10^{-3}, Fig. 2E, GM_P-GM_{Ppre}).

Table 1. Patient and tissue sample characteristics. Paired malignant and nonmalignant tissue biopsy samples were extracted from the radical prostatectomy specimens by an experienced uropathologist. Age, total serum prostate specific antigen (PSA) and percentage of free PSA (fPSA) values were determined at the time of tumor diagnosis. Tissue biopsy wet mass used in high-resolution respirometry (HRR) was determined prior to the transfer of extracted tissue samples into the O2k chambers. Tumor histology characteristics of radical prostatectomy specimens (Gleason scores of tissue samples and pathological stages) were determined using routine histopathological procedures. Data represent mean ± SD, median (age), range or quantity and percentage, respectively.

age [a]	62.7 ± 8.0 (39.9 – 73.4)
PSA [ng·mL^{-1}]	12.7 ± 27.2 (2.0 – 181.6)
fPSA [%]	14.3 ± 5.8 (3.6 - 28.1)
prostate weight [g]	44 ± 14 (20 - 79)
pathological stage, *N*(%)	
pT2 (localized)	25 (50.0)
pT3 (extracapsular extension)	21 (42.0)
pT4 (invasion into adjacent structures)	4 (8.0)
tumor histology PCa tissue samples, *N* (%)	
Gleason score 6 (patterns 3+3)	11 (22.0)
Gleason score 7 (patterns 3+4)	9 (18.0)
Gleason score 7 (patterns 4+3)	21 (42.0)
Gleason score 8 (patterns 5+3)	1 (2.0)
Gleason score 9 (patterns 4+5)	6 (12.0)
Gleason score 10 (patterns 5+5)	2 (4.0)
tissue sample wet mass [mg]	
benign	6.49 ± 1.48
malignant	6.51 ± 1.46

Stratification of tumors according to their risk potential revealed that the differences in OXPHOS capacities were mainly driven by the high grade tumors in our sample cohort (Gleason score >7) (Fig 1F,G). Whereas relative respiration (*FCR*, respiratory rates normalized for the internal reference state NS_E) of low grade tumors (Gleason score ≤7) was similar to benign tissue, it was significantly different in the high grade tumors (Fig. 1F). A direct comparison of specific O_2-fluxes in low and high grade tumors confirmed a significant reduction of N-pathway respiration (Fig. 2G – effects of ADP and rotenone) and increase of pyruvate

and especially succinate respiration (Fig. 2G – effects of pyruvate and succinate) in the high grade tumors. Altogether, HRR analysis of paired benign/cancer tissue samples uncovered a substrate shift for respiration from glutamate&malate to succinate and to a lesser extent pyruvate in prostate tumors, particularly in the high grade tumors, and higher vulnerability of tumors by oxidative stress.

Several control experiments were performed to secure the validity of our HRR SUIT protocol. Control experiments with split tissue samples (*N*=6) analyzed with or without the oxidative stress step indicated a consistent difference through all post-treatment coupling- and pathway-control states, including the succinate pathway and cytochrome c oxidase activity (SI Fig S1A). O_2-flux differences were reduced only for the oxidative stress step, while the stimulatory effects of pyruvate, succinate and uncoupling, and the inhibitory effect of rotenone remained unchanged (SI Fig. S1B). Along the same lines, analysis of N- and NS-pathway capacities and the relative effects of succinate, uncoupler or rotenone on respiration in six paired benign and malignant samples using a protocol without H_2O_2 treatment confirmed that the observed alteration in PCa tissue was not compromised by oxidative stress treatment (SI Fig S1C,D). Although the extent of inhibition of O2-flux by oxidative stress in paired tissue samples was higher in tumor tissue, the extent of inhibition was consistent through all substrate/coupling states within the benign and the malignant samples compared to samples subjected to the SUIT protocol without an oxidative stress step (SI Fig. S1E). Finally, measurement of the single enzymatic step of Complex IV using a protocol with inhibition of CI, CII and CIII, revealed the same impact of oxidative stress as for all coupling- and pathway-control states, indicating that CIV also was not specifically inhibited by H_2O_2 (SI Fig –S1F, compare to S1E-BE).

In an additional control experiment comparing benign/benign paired samples we confirmed that observed respiratory differences between benign and malignant samples were not caused by tissue heterogeneity or sampling bias. Twenty paired benign/benign samples subjected to the same analysis protocol as benign/malignant samples showed no differences (SI Fig S2A-C). Also, when grouping benign samples based on their zonal origin (medial or posterior peripheral zone or transitional zone) we found no difference in either absolute or normalized N- or NS-pathway capacities (SI Fig S2C-E).

Increased mtDNA mutation load in primary human prostate cancer tissue

Following HRR experiments, we deep sequenced the mtDNA genome via NGS to explore the mtDNA landscape of our samples (Fig. 1A) and assessed a potential link of respiratory control patterns and heteroplasmies (HPs) in ET-proteins or tRNA coding regions. Details of all 147 heteroplasmies found across the entire sample pool, including their presence and pathological context as listed in MitImpact 2.9 database (Castellana et al., 2017), are presented in Table S3. Private mutations, defined as HPs found only in one tissue type, were more frequent in the cancerous samples (Fig. 3A). In benign samples a total of 33 private HPs were found compared to 84 in the malignant tissues. Significantly more HPs found in cancer tissue were located in the coding region (72 vs 23, O.R.=2.7, p=0.007), whereas the number of HPs in the non-coding control region was similar (10 vs 12) reflecting an accumulation of HPs especially in the coding mt-genome of the tumors (Fig. 3B). In addition, a higher number of non-synonymous HPs in all ET-protein-coding mtDNA regions (MT-ND1-6=CI, MT-CO1-3=CIII, MT-CYB=CIII and MT-ATP6-8=F_OF_1 ATPase) were detected in malignant compared to the paired non-malignant benign tissue samples (38 vs 10) while the number of mt-tRNA mutations (MT-T=tRNA) was equal (2 vs 2, Fig. 3C). 35 heteroplasmy sites in the PCa samples showed an allele frequency (AF) >10% compared to only 11 in the benign samples, while 15 of the HPs detected in the malignant samples showed an AF>50% compared to only 5 in the benign tissue (Fig. 3D). Consequently, overall HP levels were significantly higher in malignant tissue in comparison to the benign tissue (p=0.03, Fig. 3E). Almost half (46%) of the tumor samples harbored ≥2 HPs while 60% of the benign samples harbored no HP (Fig. 3F). The number of HPs per mt-gene was correlated to gene size as shown for MT-ND genes (r^2=0.87, p=0.004, Fig. 3G), suggesting no cancer-specific mutational “hotspots” in primary human PCa.

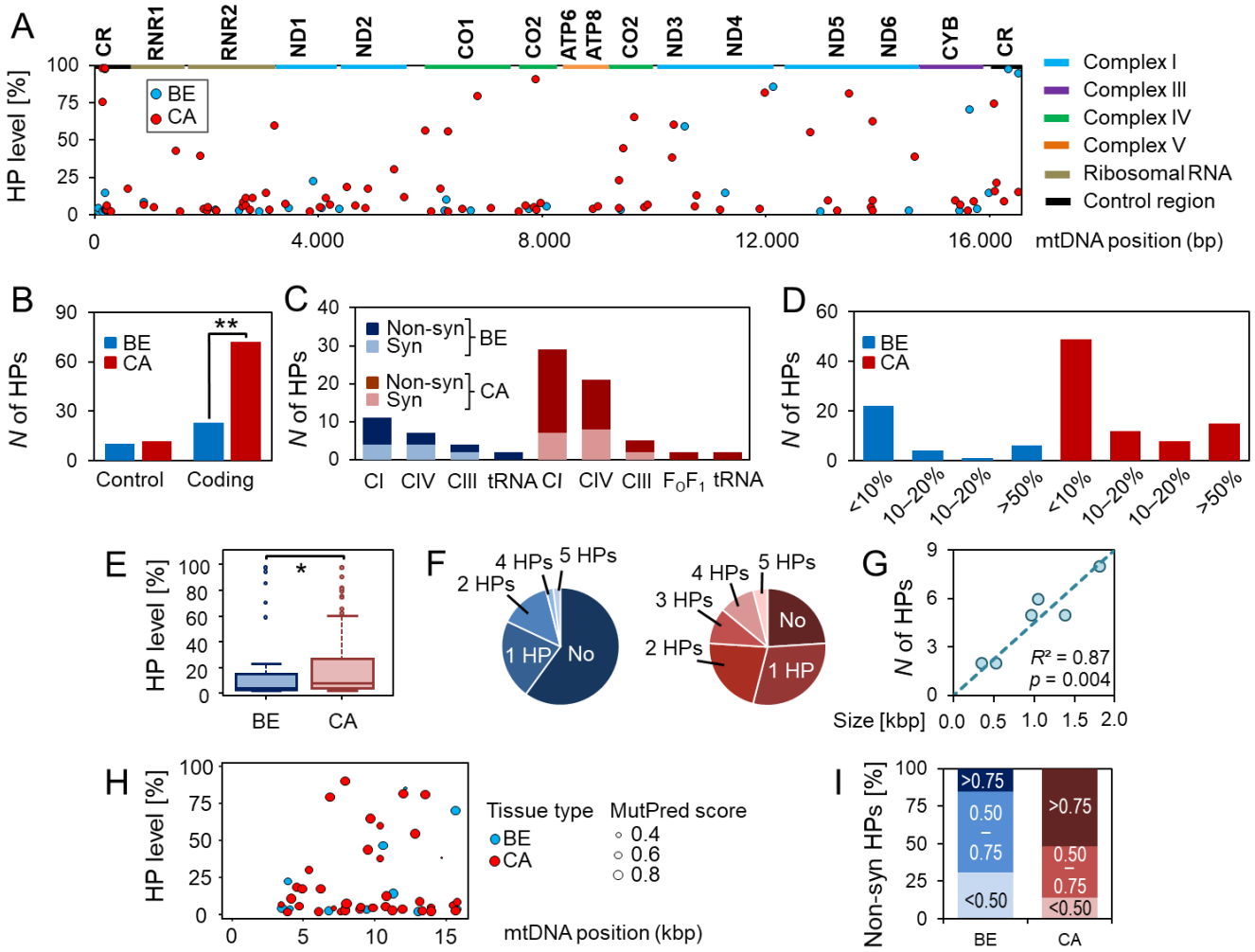

Fig. 3. mtDNA heteroplasmies in benign and malignant prostate tissue samples. A. Levels and locations of HPs in benign (blue) and malignant (red) samples across indicated loci of the entire mtDNA. The regions shown include both the non-coding control region (CR) as well as the 13 protein coding genes, marked by colored boxes. ND, CO and ATP refer to genes coding for subunits of Complex I (CI; NADH:ubiquinone oxidoreductase), Complex IV (CIV; ferrocytochrome c:oxygen oxidoreductase and ATP synthase, respectively, whereas CYB encodes a subunit of Complex III (CIII; ubiquinol:ferricytochrome *c* oxidoreductase). **B.** Total count of private mutations, located in either the non-coding D-loop or coding areas of the mt-genome in benign and malignant tissue, respectively. **C.** Incidence of synonymous (Syn) vs non-synonymous (Non-syn) HPs located in protein coding sequences (F_OF_1-ATP synthase=CV; tRNA genes=tRNA) found in either benign (blue) or malignant (red) tissue samples. **D.** Detailed proportions of samples harboring variants with defined HP levels (<10%, 10-20%, 20-50% and >50%) in the benign (blue) and cancerous (red) samples. **E.** Boxplot of HP levels comprising all (synonymous and non-synonymous) heteroplasmies in benign and malignant tissue samples. **F.** Numbers of HPs found per sample in benign (blue circle) and the malignant (red circle) samples. **G.** Correlation of gene size in kbp to HP count as detected in the mt-ND genes. **H.** MutPred Pathocenicity Scores of all non-synonymous HPs in benign (blue) and malignant samples (red) identified across the entire mtDNA. The size of the spots indicates the likely functional effects **I.** Proportion of benign and malignant samples carrying HPs with defined MutPred Pathogenicity scores reflecting their likely functional effect.

Of all non-synonymous mutations in protein coding regions, only two variants (T15719C and T10551C) have been previously detected in human cancers and only two variants were associated with a specific clinical phenotype, *e.g.*, maternally inherited diabetes-deafness syndrome (MIDD; G3421) and developmental delay, seizure and hypotonia (G4142A) according to MitoMap (Table S3). Of these mutations, only the T10551C mutation, which leads to a substitution at amino-acid position 28 (S28P) of the ND4L protein, exhibited a high HP

level (58%) while the other variants listed in MitoMap all exhibited allele frequencies below 20%. Of the four samples harboring mutations in mitochondrial tRNA (MT-T) coding genes (Table S3 and SI Fig. 4), only one variant (G15995A, MT-TP, $tRNA^{Pro}$) has been previously detected in a patient suffering from cystic fibrosis (Wong et al., 2002) and was also classified as "likely pathogenic" by the MitoTIP prediction tool (https://www.mitomap.org/cgi-bin/mitotip). This mutation leads to a G>A substitution in a highly conserved region of the anticodon-stem, resulting in a base-pair mismatch with likely effect on RNA folding and stability (SI Fig. S4). However, the frequency of this tRNA variant (15%) will most certainly not impact mt-function in a significant way as previously demonstrated for the well characterized mitochondrial $tRNA^{(Leu(UUR))}$ mutation associated with mitochondrial encephalomyopathy, lactic acidosis, and stroke-like episodes (MELAS) (Mazat et al., 1997).

Table 2. Non-synonymous mtDNA mutations of samples chosen for mRNA expression profiling via next-generation sequencing. mtDNA mutation profile of the PCa subgroup selected for expression profiling. In the "low GM-pathway OXPHOS (GM_P) capacity, severe phenotype" subgroup, five out of eight samples harbored non-synonymous mtDNA mutations in genes encoding for mitochondrial CI subunits, while only one sample in the "high GM_P mild phenotype" subgroup showed a potentially deleterious mutation (in MT-ND3). Mt-position: location of HP according to the rCRS; HP: type of nucleotide substitution; HP level [%]: Level of detected nucleotide substitution compared to the rCRS; Gene ID: mt-gene affected by detected HP; AA subst: type of amino acid substitution caused by the mutation.

Sample ID	GM_P	Mt-position	HP level [%]	Gene ID	AA subst
PK_28_CA	high	9460	44.1	MT-CO3	L85P
PK_34_CA	high	10326	3.8	MT-ND3	S90P
PK_65_CA	high	7589	2.1	MT-CO2	A2T
	high	15719	8.7	MT-CYB	Y325H
PK_44_CA	low	5359	30.2	MT-ND2	I297T
	low	13916	2.5	MT-ND5	G527E
PK_50_CA	low	7986	7.7	MT-CO2	R134Q
PK_54_CA	low	3850	2.2	MT-ND1	A182T
	low	4896	17.4	MT-ND2	Y143H
	low	13288	2.6	MT-ND5	G318S
PK_62_CA	low	10731	5.5	MT-ND4L	D88N
PK_80_CA	low	9010	54.0	MT-ATP6	A162T
	low	13886	5	MT-ND5	L517P
PK_82_CA	low	10353	60.2	MT-ND3	A99T

In order to estimate and compare the potential functional relevance of the mtDNA variants detected in benign or malignant samples in our study, we determined the MutPred Pathogenicity score (Mort et al., 2010) for all non-synonymous HPs (Fig. 3H). This score yields robust predictions when used for mtDNA mutations (Pereira et al., 2011). While only 14% of HPs of benign sample exhibited a high MutPred Score (>0.75), half of all HPs of the cancerous samples fall into this category (Fig 3I).

Non-synonymous mtDNA mutations are a hallmark of high-grade tumors

To evaluate a correlation of clinical parameters and mtDNA mutation frequency in primary human PCa tissue, a logistic regression analysis was performed (Table S4). Overall mtDNA mutation load (non-coding, synonymous and non-synonymous) correlated significantly with increasing patient age (p=0.04), which is in line with recent reports (Ju et al., 2014;

Kalsbeek et al., 2017), and with lower free to total PSA ratios (fPSA%, p=0.04) (Table 3). The latter is of interest since a low value is a prognostic indicator of poor disease outcome (Stenman et al., 2005). While a correlation trend was detected for pT stage (p=0.08), we found no statistically significant association with histological tumor (Gleason) grade or total serum PSA, contrary to previous findings (Kloss-Brandstatter et al., 2010). When looking only at non-synonymous mtDNA mutations, however, their frequency correlated with high-grade staging (Gleason>7, p=0.02) and again with a lower free to total PSA ratio (fPSA%, p=0.04). Interestingly, non-synonymous mutations correlated negatively with patient age (p=0.06), indicating that, in contrast to the overall mtDNA mutation burden, non-synonymous heteroplasmies with a potential impact on ET-function tend to accumulate in younger patients presenting with unfavorable characteristics like high-grade tumors and low free to total PSA ratios.

Deleterious mtDNA mutation load is correlated to OXPHOS capacity

While increasing numbers of potentially deleterious mtDNA mutations in cancer samples are reported (Petros et al., 2005; Arnold et al., 2009; Kloss-Brandstatter et al., 2010; Lindberg et al., 2013; Hopkins et al., 2017), the functional significance of these alterations is rarely evaluated. Based on mt-function and the mtDNA sequence analyzed in each sample, we correlated the functional data with the frequency and type of mtDNA mutations. We considered only non-synonymous (missense or nonsense) mutations in genes relevant for the assembly or function of the OXPHOS machinery (MT-ND, MT-CO and MT-CYB genes) as potentially deleterious mutations with a likely impact on OXPHOS and ATP production. Samples carrying non-synonymous HPs in protein encoding genes showed a significant decrease of relative GM-pathway capacity in both the benign (p=0.005) and malignant (p=0.004) samples (Fig 4A). In contrast, mutations in the non-coding control region of the mt-genome had no effect (Fig. 4B). GM-pathway capacity was reduced only in samples carrying non-synonymous mutations in CI genes (MT-ND1-6) but not in those encoding for CIII or F_OF_1-ATPase proteins (COI-III, CYB and ATP6-8) (p=0.0004; Fig 4C).

Table 3A: Metagenes representative for the severe respiratory phenotype tumor cohort. Significantly overexpressed genes exhibiting a significant correlation (r>0.4, p<0.05) were extracted from the "severe" phenotype samples and classified as representative "metagenes" for this cohort by applying the procedure described recently (Angelova et al., 2015).

Table 3A: Severe respiratory phenotype metagenes

Gene ID	Gene name
ACADL	Acyl-CoA dehydrogenase long chain
ALDH7A1	Aldehyde dehydrogenase 7 family member A1
AUH	AU RNA binding methylglutaconyl-CoA hydratase
BPHL	Biphenyl hydrolase like
CHDH	Choline dehydrogenase
CRLS1	Cardiolipin synthase 1
FECH	Ferrochelatase
LDHD	Lactate dehydrogenase D
MAOA	Monoamine oxidase A
MIPEP	Mitochondrial intermediate peptidase
NUDT8	Nudix hydrolase 8

Table 3B. Univariate and multivariate Cox analyses of patients listed in various independent prostate cancer cohorts. Data were downloaded from public servers (TCGA Data Portal https://cancergenome.nih.gov/cancersselected/prostatecancer and Gene Expression Omnibus (https://www.ncbi.nlm.nih.gov/geo/). Univariate and multivariate Cox regressions were calculated as described previously (Angelova et al., 2015).

Table 3B. Univariate and multivariate Cox Hazards analysis of prostate cancer mRNA expression cohorts

Cohort	Variables	Univariate Cox model		Multivariate Cox model	
		HR (95% Ci)	*p*	HR (95% Ci)	*p*
GSE16560	age			1.05 (1.03-1.08)	<0.001
(*N*=281)	Gleason score			1.81 (1.60-2.06)	<0.001
	severe phenotype metagenes	0.61 (0.44-0.84)	0.002	0.92 (0.81-1.03)	0.139
GSE40272	PSA			1.03 (0.99-1.08)	0.1574
(*N*=84)	T staging			4.18 (1.17-14.92)	0.028
	N staging			7.51 (1.78-31.79)	0.006
	severe phenotype metagenes	0.48 (0.19-1.23)	0.120	1.23 (0.58-2.60)	0.591
GSE70768	age			0.80 (0.95-1.12)	0.412
(*N*=111)	PSA			1.03 (0.76-1.04)	0.156
	T staging			0.89 (0.58-8.17)	0.248
	Gleason score			2.18 (1.85-8.17)	0.002
	severe phenotype metagenes	0.31 (0.1-0.94)	0.029	4.98 (0.29-2.19)	0.659
GSE70769	Gleason score			2.11 (1.50-2.97)	<0.001
(*N*=94)	PSA			1.01 (1.50-2.97)	0.511
	T staging			1.47 (0.97-1.06)	0.100
	severe phenotype metagenes	0.29 (0.12-0.57)	<0.001	0.53 (0.29-0.96)	0.037
PRAD-TCGA	PSA			1.02 (0.98-1.05)	0.338
(*N*=497)	T staging			1.72 (1.03-2.86)	0.037
	N staging			0.83 (0.49-1.43)	0.508
	Gleason score			2.03 (1.56-2.65)	<0.001
	severe phenotype metagenes	0.53 (0.32-0.89)	0.0014	0.61 (0.44-0.84)	0.034

Already moderate levels of deleterious mtDNA mutations in CI genes can lead to significant functional and clinical effects (Kirby et al., 2003; McFarland et al., 2004). To evaluate the impact of increasing HP levels in MT-ND genes on CI-function in detail, we divided malignant samples into subgroups exhibiting a HP level of either 30-60% or >60%. A higher HP level was associated with a more pronounced reduction in respiratory N-pathway capacity (depending on CI) and correspondingly with a higher proportion of S-pathway capacity to retain full aerobic ATP production (Fig. 4D). In the samples exhibiting the highest HP loads (>60%, *N*=4), N-mediated respiratory capacity with glutamate&malate was reduced to 16% of total NS-mediated OXPHOS capacity. To highlight compensation in samples exhibiting high levels of CI mutations, we compared the N- and S-pathway capacities in samples harboring high levels of non-synonymous HPs in either CIV or CI only (Fig 4F). While the N-pathway capacity was similarly low, oxygen consumption supported by succinate was significantly higher in the group harboring CI mutations (p=0.002) indicating that a defect in CIV will inevitably affect total respiration, while defects in CI can be sufficiently compensated by an increase in S-pathway capacity.

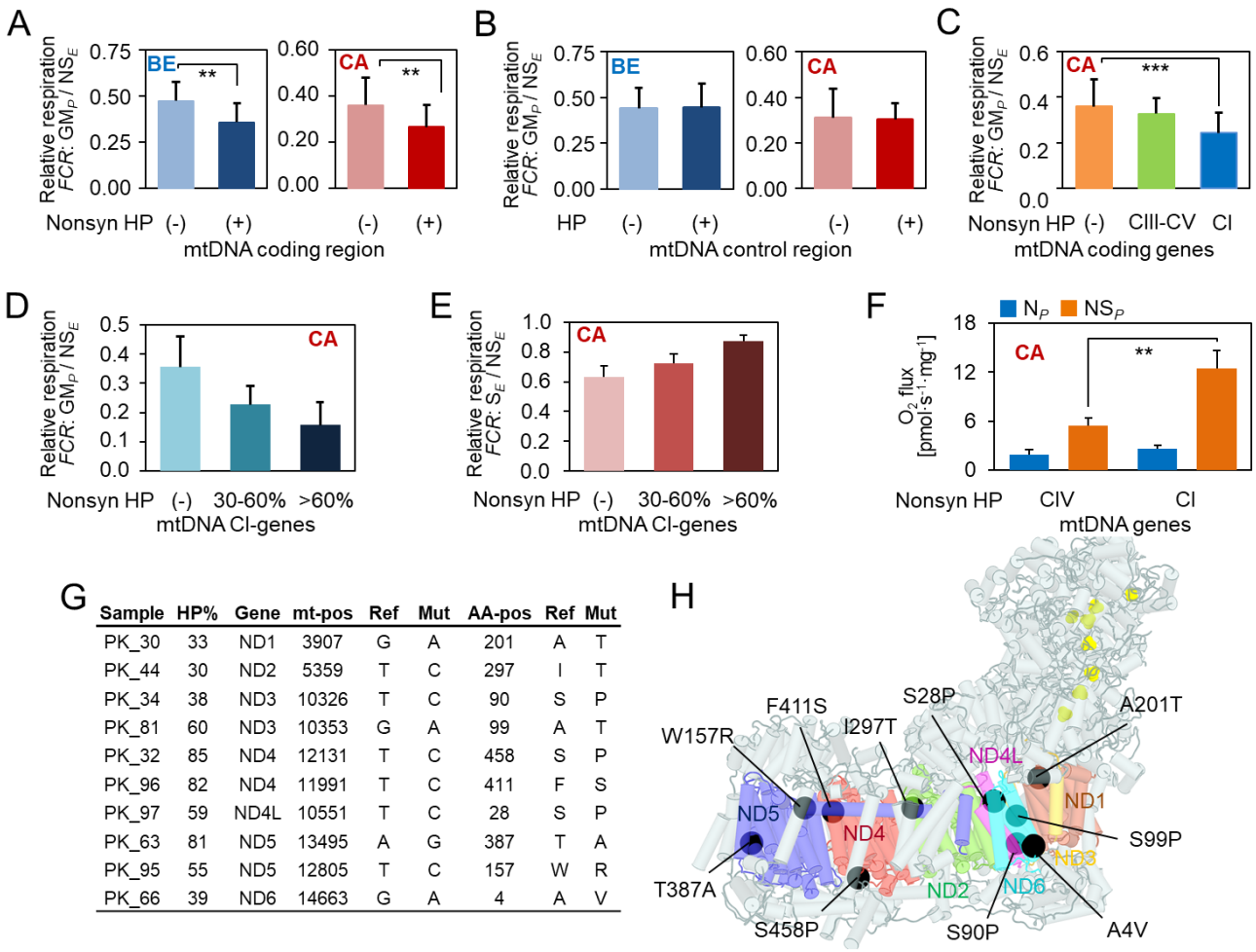

G

Sample	HP%	Gene	mt-pos	Ref	Mut	AA-pos	Ref	Mut
PK_30	33	ND1	3907	G	A	201	A	T
PK_44	30	ND2	5359	T	C	297	I	T
PK_34	38	ND3	10326	T	C	90	S	P
PK_81	60	ND3	10353	G	A	99	A	T
PK_32	85	ND4	12131	T	C	458	S	P
PK_96	82	ND4	11991	T	C	411	F	S
PK_97	59	ND4L	10551	T	C	28	S	P
PK_63	81	ND5	13495	A	G	387	T	A
PK_95	55	ND5	12805	T	C	157	W	R
PK_66	39	ND6	14663	G	A	4	A	V

Fig. 4. Correlation of mtDNA heteroplasmies and respiratory capacities. A. Relative GM-OXPHOS respiratory capacity with glutamate&malate (GM_P/NS_E) in benign (blue) or malignant (red) samples carrying either no or only synonymous HPs (-) (N_{BE}=36 and N_{CA}=23) versus samples carrying non-synonymous HPs (+) (N_{BE}=14 and N_{CA}=27) in the coding regions of the mt-genome. **B**. Comparison of relative GM-OXPHOS capacity in samples without mutations (-) (N_{BE}=38 and N_{CA}=37) versus samples with mutations (+) (N_{BE}=12 and N_{CA}=13) within the non-coding (control) region of the mt-genome. **C.** Impact of location of non-synonymous HPs on relative GM-OXPHOS capacities. Tumor tissue samples were categorized according to no HPs (-) (orange; *N*=24), and HPs located in genes encoding proteins of CIII – CV (CO, ATP, CYB; green; *N*=10) or in genes encoding proteins of CI (ND1 – ND5; blue; *N*=20). **D,E.** Relative GM-OXPHOS (GM_P/NS_E, D) and relative S-ET system (S_E/NS_E, E) respiratory capacities in malignant tissue samples harboring non-synonymous HPs in CI-coding mt-genes. Tumors were grouped into samples carrying no non-synonymous HPs ((-); *N*=23), samples with variant levels of 30-60% (30-60%; *N*=6) and samples with variant levels >60% (>60%; *N*=4). **F.** N-pathway (blue) and S-pathway (orange) respiratory capacities in malignant samples harboring high-level (>60%) synonymous HPs in either CIV-coding genes (*N*=4) or CI-coding genes (*N*=4). **G.** List of malignant samples carrying non-synonymous variants with HP levels >30% (HP%= heteroplasmy levels, Gene= mt-gene, mt-pos= location of variant on mtDNA sequence, Ref= nucleotide in rCRS sequence, Mut= altered nucleotide found in sample, AA-pos= position of encoded amino-acid in protein sequence, Ref= amino-acid in wild-type protein, Mut= altered amino acid). **H.** Structure of human respiratory Complex I and location of mutations found in this study. mtDNA-encoded CI-subunits (ND1-6) are shown in colors (ND1=dark red, ND2=light blue, ND3=orange, ND4=red, ND4L=purple, ND5=dark blue and ND6=light blue), mutations are shown as black circles and Fe-S clusters as yellow spheres. To visualize mutation sites see complemental iSee package using any JavaScript enabled web browser (http://www.ruppweb.org/ICM/).

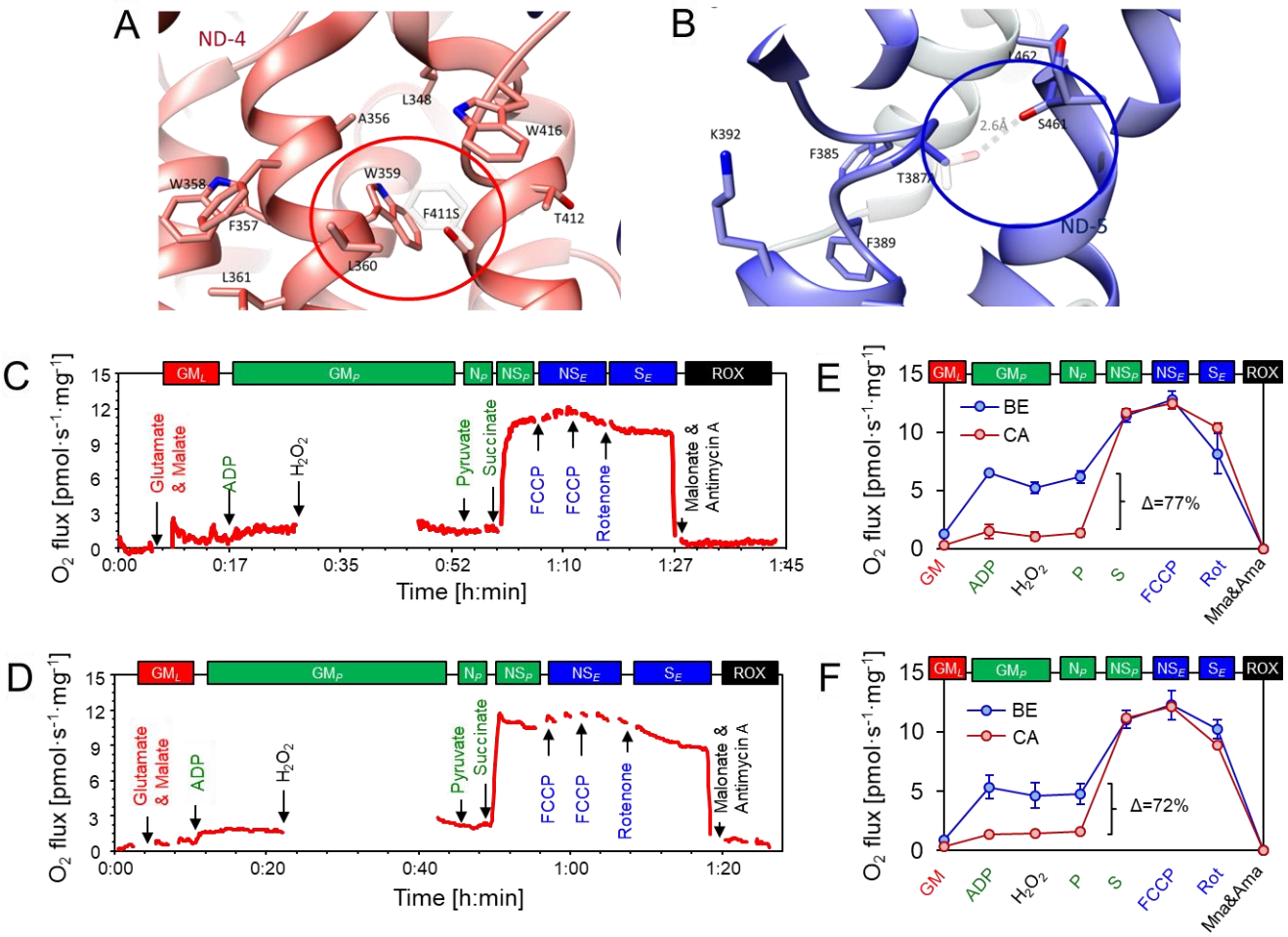

Fig. 5. Structural analysis and respiratory function of two malignant samples carrying a high HP level, non-synonymous mtDNA mutation in a CI gene. A. Structural change caused by the F411S mutation (red circle) in ND4. Wild-type (F) and mutated variant (S) are depicted and superimposed together with amino-acid residues involved in the hydrophobic interaction network of the α-helix structure (W359, L360 and W416, respectively). **B.** Structural change caused by the T387A mutation located within the loop of the discontinuing helix 12 in the central axis of CI membrane domain (blue circle) in ND5. Wild-type (T) and mutated variant (A) are superimposed and the stabilizing hydrogen bond present in the wild-type protein is depicted by a scattered line. **C-D**. HRR experimental traces of the malignant biopsies carrying the F411S mutation (**C**) or the T387A mutation (**D**), respectively. The red line represents wet mass-specific O_2 flux (oxygen consumption [pmol s^{-1}·mg^{-1}]). **E-F.** Respiratory capacities of malignant samples (red) carrying either the F411S mutation (**E**) or the T387A mutation (**F**), and the corresponding benign tissue (blue). Values represent mean ± SD of the two separate experiments for each tissue sample. See Fig. 2 and Tables S1 and S2 for abbreviations. Refer to legend of Fig. 2 for description of coupling states and SUIT protocol.

A structural basis for the effect of CI mutations

To characterize the molecular and biochemical mechanisms by which the CI-mutations detected in our samples could affect respiratory N-pathway capacity, an in-silico assessment of the potential structural changes in CI was performed, considering mutations exhibiting critical HP-levels of ≥30% (Fig 4G,H). We analyzed the structural basis for the effect of functionally relevant mutations on the basis of the CI subunit in the recently published cryo-EM structure of the human respiratory supercomplex SC $I_2III_2IV_2$ (Guo et al., 2017). The majority of the identified mutations cluster near the charged central axis of CI (Fig 4H, online supplemental iSee package, http://www.ruppweb.org/ICM/). This is of significance, since structural analysis suggested that this region is at the center of the Q-cycle redox coupling and is crucial for the translocation of protons across the mt-inner membrane (Baradaran et al., 2013).

To illustrate potential structural consequences of the mutations, two examples exhibiting a very high (>80%) variant level and severe alteration of the HRR profile (Fig. 5) were examined in detail: The first variant (T11991C) has recently been detected in a prostate cancer tissue sample of the TCGA PRAD-US cohort (Cosmic ID: COSM1132242, https://cancer.sanger.ac.uk/cosmic/mutation/overview?id=1132242). It leads to the substitution of a large hydrophobic, aromatic amino acid with a small, polar amino acid (F411S). The substitution is located within a hydrophobic region, consequently interrupting a hydrophobic interaction network based on Pi-Stacking between conserved helices in the ND4 domain of CI (Fig. 5A). The second variant (A13495G) is located in the ND5 gene leading to the loss of a polar residue within the loop of the discontinued helix 12 in the central axis of the CI membrane domain (T387A). This part of the structure was annotated as flexible region that might play an important role initiating local conformational changes necessary to position corresponding key residues in the central axis (e.g. K392) during proton pumping (Baradaran et al., 2013). As illustrated in Fig 5B, a hydrogen bond is lost due to the T387A mutation in this important region. HRR analysis of these samples revealed that N-pathway capacity (PGM; pyruvate&glutamate&malate) constituted only a marginal fraction (<10%) of combined NS-driven respiration (Fig. 5C,D). Importantly, N-pathway capacity in the malignant tissue biopsies harboring these two high-level variants was decreased by more than 70% in comparison to their corresponding benign tissues (Fig. 5E,F), supporting the hypothesis that these mutations play a causal role for the observed phenotypes.

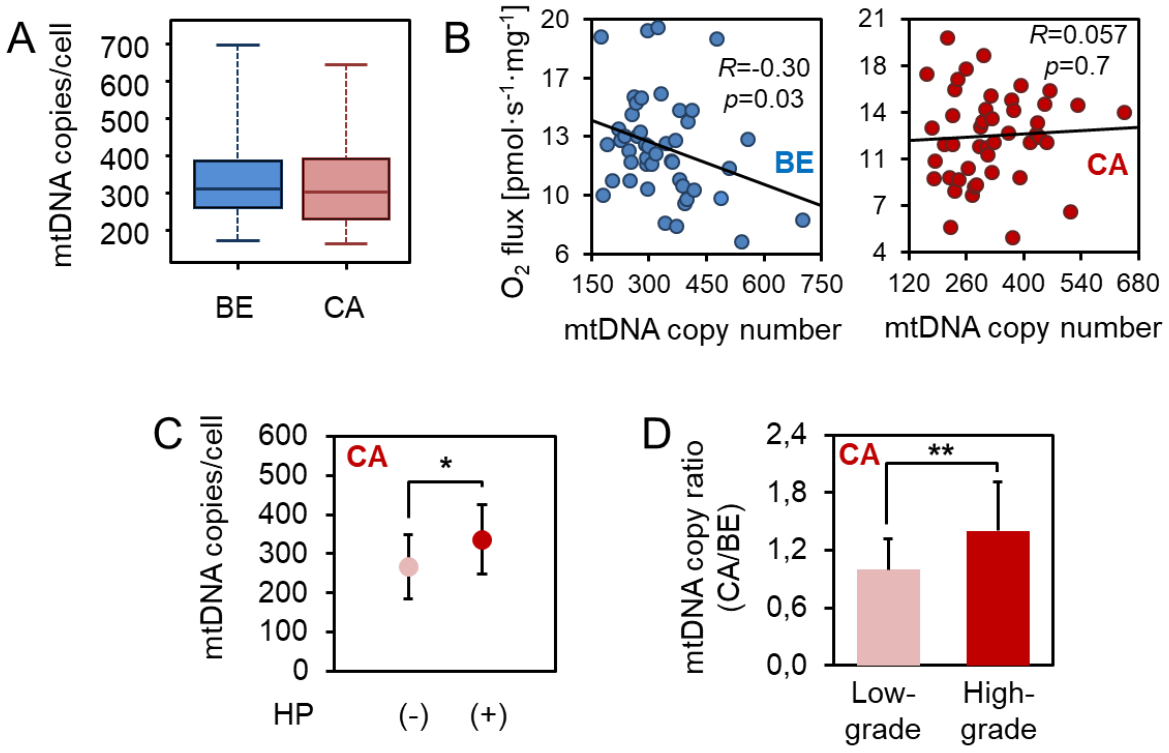

Fig. 6. mtDNA copy number load in malignant and benign prostate tissue samples. A. Boxplot of mt-CN ratios (CA/BE) per cell in the benign (blue) and malignant (red) tissue samples. **B.** Correlation of maximal NS-ET capacity (y-axis) and mt-CN (x-axis) in benign (BE, blue circles) and malignant tissue (CA, red circles). **C.** Mean mt-CNs ± SD in malignant samples without ((-), light red, *N*=17) or with ((+) dark red, *N*=33) mtDNA mutations, respectively. **D.** Comparison of mt-CN ratios ± SD calculated as $mt\text{-}CN_{CA}/mt\text{-}CN_{BE}$ in tumor samples in low grade (Gleason score ≤7, light red, *N*=40) *vs* high grade (Gleason score >7, dark red, *N*=10).

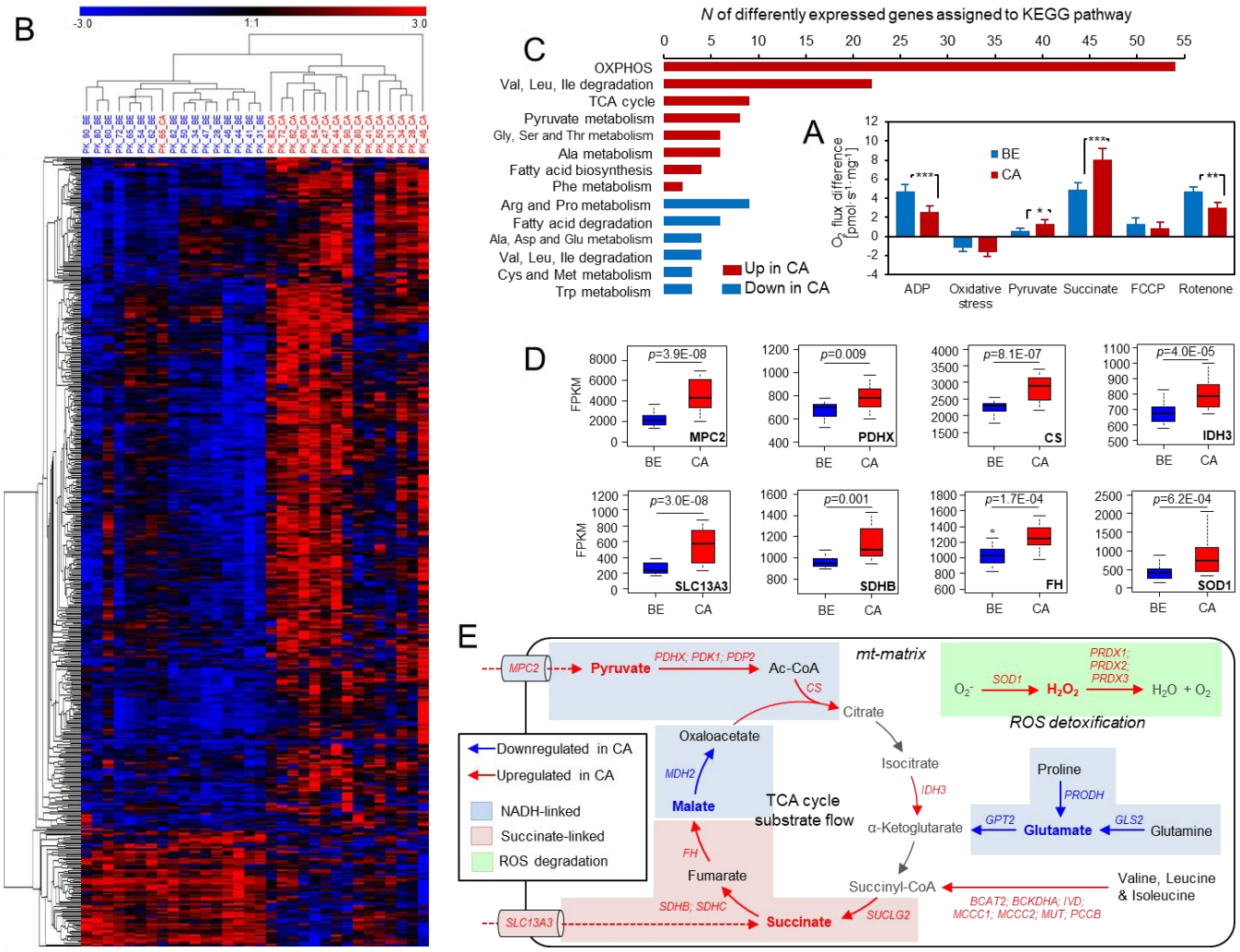

Fig. 7. Differential mRNA expression of mitochondrial genes and enriched metabolic KEGG pathways in 16 paired tissue samples. A. Respiratory characteristics of tissue samples for which RNA-seq expression analysis was performed. Shown are the effects of substrates glutamate&malate, pyruvate, succinate, oxidative stress, uncoupler FCCP, and CI inhibitor rontenone on O_2-flux in benign (blue) and malignant (red) tissue samples. **B.** Heatmap and hierarchical clustering of all significantly differentially expressed mitochondria-related genes (*FDR*<0.01) based on the MitoCarta2.0 Gene Catalog in the benign (blue) or malignant (red) tissue samples. **C.** Enriched metabolic KEGG pathways upregulated (red) or downregulated (blue) in cancer tissue based on the InnateDB pathway overrepresentation analysis of all differentially expressed mt-related genes. **D.** Boxplots representing Fragments Per Kilobase Million (FPKM) values for expression of significantly increased metabolic key-enzymes in the malignant (red) vs the benign (blue) tissue samples. **E.** Detailed annotation of single up-regulated TCA-cycle key-enzymes in the benign (blue arrows) and cancerous (red arrows) samples. Blue boxes mark steps mainly involved in NADH-linked electron transfer, red boxes highlight steps related to succinate-linked electron transfer, and green boxes mark steps involved in ROS detoxification. Substrates used during the respirometry experiments (malate, glutamate, pyruvate, succinate) are indicated in bold type while blue or red colored names and arrows mark enzymes and enzymatic reactions that are higher in either benign or malignant samples, respectively. Full names of enzymes are given in the main text. Values represent mean ± SD unless otherwise stated.

Increased mtDNA copy numbers in high grade prostate cancer tissue

Having found significant differences in mt-bioenergetics and mtDNA mutations between benign and malignant prostate tissue and because the effect of mtDNA copy number (mt-CN) on mt-function in primary prostate cancer tissue is still poorly understood, we examined whether differences in (mt-CN) number might be associated with mitochondrial function,

mtDNA mutational burden or disease stage. mt-CN was assessed by a standard-corrected duplex real-time quantitative PCR (qPCR) (Fazzini et al., 2018). Median mt-CN load was 310 per nuclear genome (range: 172 – 698) in the benign and 303 (range: 143 - 645) in the malignant tissue samples, indicating no meaningful difference (Fig. 6A). While it has been proposed that mt-CN constitutes a reliable marker for mitochondrial protein density and OXPHOS capacity in general (Paglialunga et al., 2012), we found a negative correlation between mt-CN and OXPHOS capacity in the benign tissue (R=-0.30, p=0.03) and no correlation in the malignant tissue (R=0.057, p=0.7; Fig 6B). When looking at the PCa samples harboring potentially deleterious mtDNA mutations, we found significantly higher mt-CNs compared to samples carrying no HPs (p=0.03; Fig 6C). We identified a significant increase of mt-CN ratios in the high-grade (Gleason score >7) tumors when compared to low-grade (Gleason score ≤7) tumors (p=0.002; Fig. 6D). This suggests an increase of mtDNA load with increasing malignancy and the presence of potentially deleterious mtDNA mutations.

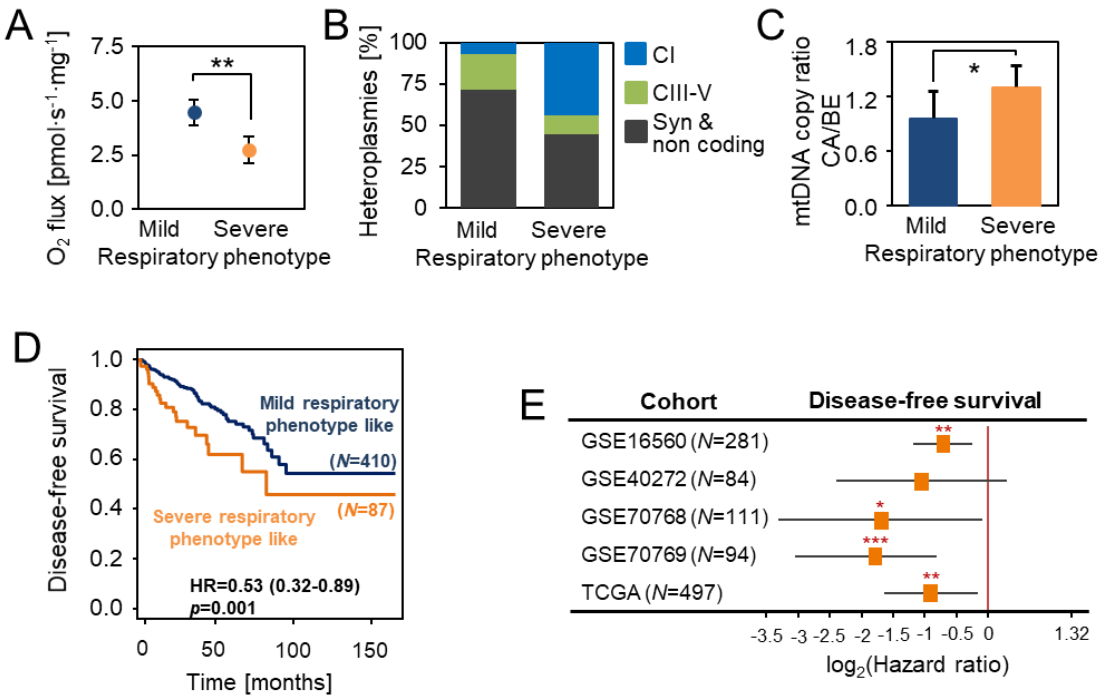

Fig. 8. Association of PCa tissue samples exhibiting a severe respiratory phenotype with disease-free survival employing a highly correlated metagene set. A. Glutamate&Malate-linked OXPHOS capacity (GM_P) in the severe (orange) versus mild (blue) respiratory phenotype PCa tissue samples. **B.** Relative proportion of synonymous/non-coding (grey), non-synonymous CIII-IV (green) and non-synonymous CI (blue) mtDNA mutations detected in samples of the mild and severe respiratory phenotype cohorts, respectively. **C.** mt-CN ratios (CA/BE) as determined by duplex qPCR in the severe (orange) versus mild (blue) respiratory phenotype PCa samples. Values represent mean ± SD. **D,E.** A metagene set of 11 genes (Table 6) highly correlated to the gene expression profile of the severe respiratory phenotype PCa samples was used to dichotomize 5 PCa sample cohorts into samples exhibiting a mild or a severe respiratory phenotype-like metagene signature and perform Kaplan-Meier and Hazard ratio (HR) analysis of disease free survival probabilities. In the Cancer Genome Atlas prostate adenocarcinoma (PRAD-TCGA) sample set, RNA-seq was used for expression profiling, microarray analysis was used for the remaining four datasets. **D.** Disease-free survival Caplan-Meier curves for the PRAD-TCGA cohort (N=497). A HR of 0.53 (0.32-0.89, p=0.001) was calculated for this set. **E**. Disease free survival probabilities (HRs and CI intervals), for all five independent prostate cancer cohorts (N=1067). Cases exhibiting a severe respiratory phenotype-like metagene signature showed a significantly shorter DFS probability in four of the five cohorts.

Transcriptome mirrors altered OXPHOS capacity

Quantitative mRNA expression analysis via NGS was performed for 16 paired tumor/benign representative samples. These cases were selected on the basis of their mt respiratory phenotype to mirror the HRR properties of the whole sample cohort (Table S5, Fig. 7A, compare to Fig. 2G). We analyzed 1158 nuclear genes related to mitochondrial function and metabolism based on a previously proposed "MitoCarta2.0" (Calvo et al., 2016). Comparison of expression of these genes between benign and cancer tissues identified 512 differentially expressed genes (false discovery rate*, FDR* <0.01, Fig. 7B). A Pathway Over-Representation Analysis (ORA) of the differently expressed genes using the InnateDB Pathway online tool (Breuer et al., 2013) allocated differentially expressed genes to amino acid and pyruvate metabolism, TCA cycle, OXPHOS and fatty acid turnover pathways (Fig. 7C). mRNA expression of key proteins related to OXPHOS, TCA-driven pyruvate degradation and succinate provision, and of enzymes involved in ROS detoxification were upregulated in the malignant samples (Fig 7D). Expression of mitochondrial pyruvate carrier 2 (MPC2) and subunits of pyruvate dehydrogenase (PDHX and PDP2) drive mitochondrial allocation and conversion of pyruvate into either lactate or acetyl-CoA (Ac-CoA). The increased expression of citrate synthase (CS) and subunits of mitochondrial isocitrate dehydrogenase (IDH3) promotes conversion of Ac-CoA to citrate and ultimately TCA driven oxidation of pyruvate into α-ketoglutarate. Increased expression of the mitochondrial succinate transporter (SLC13A3), two succinate dehydrogenase subunits (SDHB and SDHC) along with subunits of key TCA-enzymes (succinyl-CoA synthethase, SUCLG2 and fumarat hydrogenase, FH) and enzymes involved in the conversion of various amino acids into succinyl-CoA (BCAT2, BCKDHA, IVD, MCCC1, MCCC2, MUT and PCCB) support a more efficient provision of succinate for respiration in tumors. Furthermore, the high expression of genes related to ROS degradation like superoxide-dismutase (SOD1) and peroxireductin 1-3 (PRDX1, PRDX2 and PRDX3) might indicate a higher exposure to and consequently increased necessity to detoxify mitochondrially derived oxygen radicals in tumors.

In contrast, enzymes related to glutamate driven ATP generation via the TCA-cycle (proline dehydrogenase, PRODH; glutaminase, GLS2; glutamate-pyruvate transaminase, GPT2) were downregulated in malignant compared to benign tissue. This is in line with the lower GM-pathway capacity in malignant compared to benign tissue. Genes involved in the activation and inactivation of the pyruvate dehydrogenase supercomplex (PDH), including pyruvate dehydrogenase kinases (PDK2, PDK3 and PDK4), were expressed higher in benign tissue, which suggests a more stringent regulation of pyruvate catabolism in the benign tissue. Taken together, the pathway alterations suggest a consistent pattern distinguishing benign and cancer tissue as shown in Fig. 7E.

Shorter disease-free survival of patients suffering from a severe mitochondrial respiratory PCa phenotype

We performed survival analysis using publicly available PCa cohort data annotated with disease-free survival data to evaluate the prognostic value of the specific expression pattern associated with a decrease in N-pathway respiratory capacity. We grouped HRR functional data on cancerous samples with the corresponding transcriptome profile into two equal cohorts according to their GM-OXPHOS capacity. A low GM_P ("severe") and a high GM_P ("mild") mitochondrial respiratory phenotype group was established based on the mean relative GM-OXPHOS capacity. The relative GM-respiratory capacity of the severe respiratory phenotype tumors was only about half of that of the mild respiratory phenotype tumors (Fig. 8A, p=0.002). Compared to the mild phenotype group the severe phenotype group featured a significantly higher incidence of non-synonymous mtDNA mutations, particularly in genes encoding for CI subunits (O.R.=10.4, p=0.04; Fig. 8B). Of note, five severe respiratory phenotype tumors but only one mild respiratory phenotype tumor harbored a non-synonymous CI gene mutation. The variant level in this single mild respiratory phenotype tumor was only 3.8% compared to 5.4% to 60.2% in the severely affected group of tumors (Table 2). Another distinctive property of the two groups was a significantly higher mt-CN load in the severe phenotype samples (Fig. 8C, p=0.02). We used the transcriptomic profiles to extract a metagene set of 11 genes, to test if these two distinct tumor phenotypes were associated with different disease outcomes. These metagenes were highly correlated to the severe respiratory phenotype tumors (Table 3A,

r>0.4, *p*<0.05). We then dichotomized samples from the cancer genome atlas (TCGA) prostate adenocarcinoma (PRAD) cohort (*N*=497) into two cohorts according to their metagene set expression scores using an optimum cut-off value. The high score tumor group exhibited a statistically significantly shorter disease-free survival probability (Fig 8D; HR=0.53, CI=0.32-0.89, *p*=0.001). This result was confirmed when additional 4 publicly available prostate cancer gene array expression cohorts (*N*=570) were categorized with the metagene set. Samples exhibiting a high metagene expression score, matching the expression pattern of the severe respiratory phenotype group, consistently showed lower disease-free survival probabilities in all cohorts (Fig 8E, Table 3B). Our results indicate that the prostate cancer subgroup exhibiting a distinct metabolic remodeling was associated with a more negative outcome.

Discussion

The specific metabolism of prostatic epithelial cells is characterized by secretion of citrate into the prostatic fluid. Exploiting glutamate and other amino acids as anaplerotic fuel substrates and hence as major sources for ATP production allows sparing of pyruvate for citrate synthesis and excretion. This intricate bioenergetics in benign prostate tissue has been confirmed by us previously (Schopf et al., 2016). In PCa cancer cells, the downregulation of citrate excretion (Costello and Franklin, 2016) enables the utilization of citrate for energy demands. Supporting this hypothesis, benign human prostate tissue in our study showed a significantly higher glutamate and malate-driven OXPHOS capacity while malignant tissue showed an increased utilization of mainly succinate and to a lesser extent also pyruvate to drive energy production and compensation for the reduced GM-pathway capacity. Our study on primary PCa tissue supports results obtained with PCa cell lines (Cook et al., 2012; Ippolito et al., 2016; Weber et al., 2018). A recent study of OXPHOS activity in PCa cell models demonstrated the importance of especially pyruvate to sustain malignant growth (Bader et al., 2019). In our study, the change in succinate and pyruvate preference was mainly present in high-grade tumors, indicating that this metabolic rewiring is a definitive step during tumorigenesis with prognostic significance. The shift from N- to S-pathway capacity in high-grade tumors supports the concept of substrate redirection for sparing bioprecursors for other needs while a highly efficient aerobic production of ATP is maintained from succinate through CII. These observations underscore the significance of succinate as an “oncometabolite” at the center of the TCA cycle and other important metabolic and signaling pathways in primary human cancer tissue (Tretter et al., 2016). In the light of these findings, succinate and CII are promising targets for novel anti-cancer drugs (Kluckova et al., 2013; Weber et al., 2018).

mtDNA heteroplasmy levels up to an allele frequency of 80% may exhibit only a limited functional impact on cellular energy production (Rossignol et al., 2003). Although this observation seems well supported by deleterious mtDNA mutations affecting CIV, ATP-synthase or tRNAs, like the A3243G $tRNA^{Leu}$ mutation causing MELAS syndrome or the A8344G $tRNA^{Lys}$ mutation causing MERRF syndrome (Mazat et al., 2001; Picard et al., 2014), the evidence regarding mutational threshold effects in genes leading to symptomatic CI-associated mitochondrial myopathies is in conflict with this notion. For example, bioenergetics studies on tissues obtained from clinically affected patients suffering from LHON or Leigh`s syndrome consistently show “moderate” variant levels of deleterious heteroplasmies (20 - 50%) associated with ~50% decrease in N-pathway capacity (Kirby et al., 2003; McFarland et al., 2004; Bai et al., 2000). These findings are in agreement with our study with heteroplasmy levels of 30-60% exhibiting a significant N- to S-pathway shift. Strong support for a causal link between mtDNA mutations and the respiratory alterations detected by HRR comes from the nature and location of the mutations. (*1*) Potentially deleterious mutations in mt-genes encoding CI proteins were accumulated in malignant samples exhibiting a strong N- to S-capacity phenotype. (*2*) In a high-resolution 3D model of CI, these mutations cluster to the central axis, described as a highly-charged channel involved in redox coupling and the translocation of protons (Baradaran et al., 2013). (*3*) In-silico 3D structure modeling indicates a significant structural impact by mutations such as those leading to the exchange of a hydrophobic by a polar amino acid.

An important result of our study is the finding that primary human prostate cancer tissue is highly capable of aerobic ATP production. Despite the decrease of N-pathway capacity, the cancer cells are functionally and transcriptionally “programmed” to efficiently compensate this

loss by an increase in S-linked respiration. A high respiratory capacity seems to be important for tumor initiation and metastasis as demonstrated in a breast cancer mouse model of mtDNA deficient tumor cells, which re-established respiration and tumor-initiation efficacy by horizontal transfer of mtDNA from the tumor microenvironment (Tan et al. 2015). In contrast to tumors, human skeletal muscle and human fibroblasts heavily rely on N-pathway capacity (Doerrier et al, 2018; Hung et al., 2016) and a compensatory mechanism by N to S-pathway shift is not known for mitochondrial myopathies. Ultimately, our results suggest that the immediate net effect of deleterious mtDNA mutations does not hamper cellular ATP homeostasis in primary human prostate cancer tissue. Nevertheless, the association with shorter disease-free survival and in-vitro and in-vivo data indicate that deleterious MT-ND variants increase tumorigenic potential (Gasparre et al., 2011; Park et al., 2009). This points to a tumorigenic significance of such mutations beyond the immediate effect on OXPHOS capacity and cellular energy supply.

Non-synonymous mtDNA mutations are associated with specific changes in the expression of OXPHOS-related proteins (Picard et al., 2014). In our study, gene expression pathways linked to glutamate metabolism were decreased and pathways related to pyruvate and succinate utilization were increased in tumor tissue, thus mirroring the respiratory patterns and suggesting a specific significance of such mutations. We identified a number of differentially expressed key enzymes in PCa samples that harbor higher loads of potentially deleterious mtDNA mutations. However, the mechanistic link between mutations and enzyme expression levels remains elusive at this stage. Metabolic alterations and high loads of non-synonymous mtDNA mutations are accompanied by an increase in mtDNA copy numbers, which is a characteristic of more aggressive PCa (Kalsbeek et al., 2018; Moore et al., 2017). Confirming this hypothesis, a set of highly correlated metagenes extracted from the gene expression profile of PCa samples exhibiting a severe respiratory phenotype was able to predict significantly shorter disease-free survival in PCa patients of publicly available datasets. In view of these results, we conclude that the severe NADH- to succinate-shifted respiratory phenotype provides an additional prognostic indicator for aggressive prostate cancer.

Our study has limitations: (*1*) All functional changes observed by HRR analysis were detected using artificially high concentrations of substrates and oxygen, which may lead to an overestimation of the effects. However, tissues are composed of a mixture of malignant and non-malignant cells (*e.g.*, the stroma), resulting in a “dilution” of the malignant phenotype. (*2*) The pathways evaluated by our HRR experiments involve multiple sequential enzymatic steps. Therefore, further experiments exploring isolated TCA cycle proteins and/or ETS subunits are needed to evaluate their single contribution to the OXPHOS changes observed in this study in more detail. On the other hand, our method allows a realistic evaluation of the complex interplay of the various enzymatic steps of respiration. (*3*) Only functional and genomic data were evaluated while no analyses of protein content, protein expression patterns or enzyme activities beyond mRNA expression were conducted. It is widely accepted that the combination of HRR and mtDNA sequence analysis provides the most powerful tools to study the effect of (potentially) deleterious mtDNA variants on TCA cycle and OXPHOS function (Sperl et al., 1997; Mayr et al., 2008; Valente et al., 2009; James et al., 1996). Moreover, a recent immunohistochemical study revealed a significantly elevated expression of CII-protein subunits in primary prostate cancers which is in line with our findings, indicating that elevated mRNA expression levels of CII-related genes most likely also translate into higher CII-protein content (Feichtinger et al., 2018). (*4*) More comprehensive functional characterizations of the potentially deleterious mtDNA variants described in our study are necessary to evaluate their impact on cellular ATP homeostasis. Longer patient follow-up is warranted to estimate the effects on disease outcome. Due to the prospective nature of our study, events to estimate disease outcome in our subjects are not available at this point.

In conclusion, this is the first study analyzing substrate-specific OXPHOS capacities in native primary human prostate tissue. It links remodeling of OXPHOS in prostate cancer to potentially damaging mtDNA mutations and differential expression of mitochondrial genes. Our findings suggest that a decrease in N-pathway capacity associated with potentially deleterious, high-level mtDNA heteroplasmies, primarily in mt-genes encoding CI proteins and a higher mtDNA load is a distinct characteristic of high-grade tumors, highlighting the diagnostic and prognostic potential of metabolic rewiring. Analysis of the CI molecular structure suggested a structural basis for the effects of functionally relevant mutations. Furthermore, we provide

evidence that both, potentially deleterious mtDNA mutations and an aberrant gene expression account for these alterations in a subgroup of PCa samples. We defined a severe respiratory phenotype PCa subtype that is characterized by significant alterations in N- and S-pathway capacities and show that the distinct expression signature of this subgroup is associated with worse disease prognosis in large and independent prostate cancer cohorts. This signature could thus help to identify patients at a higher risk, complementing the classical tumor grading system. Our results warrant exploring therapeutic strategies to target alterations of metabolism in prostate cancer and particularly suggests succinate-linked respiration as a therapeutic target.

Materials & Methods

Prostate Cancer Subjects

Fifty prostate cancer patients were enrolled in the study and radical prostatectomy was the first treatment in all cases (Table 1). All patients underwent surgery at the Department of Urology of the Medical University of Innsbruck. Written informed consent was obtained from all patients. The use of human prostate tissue for this study was approved by the Ethics Committee of the Medical University of Innsbruck (AN 4837) and the study was conducted in accordance with the principles of the Declaration of Helsinki. Clinical characteristics are summarized in Table 1.

Reagents

Stock solutions for the respirometry measurements were stored frozen except for the H_2O_2 titration solutions, which were prepared freshly on a daily basis. High-performance liquid chromatography (HPLC) or polyacrylamide gel electrophoresis (PAGE) grade primers, probes and barcode oligonucleotides were ordered from Microsynth (Microsynth AG, Balgach, Switzerland) as 100 µM stock solutions, stored frozen and freshly diluted prior to use.

Tissue samples and diagnostic confirmation

Tissue biopsies were extracted from prostate specimens by an experienced uropathologist using punch needles with a diameter of 3 mm. For each individual, paired tissue samples consisting of one cancerous and one non-malignant benign biopsy were collected (Fig. 1). A small portion of the biopsy was formalin-fixed, dehydrated and paraffin-embedded for subsequent diagnostic staining and validation of tissue identity, while the remaining tissue biopsy, about 13 mg wet tissue mass, was placed into pre-chilled relaxing and preservation solution BIOPS, containing 2.77 mM CaK_2EGTA, 7.23 mM K_2EGTA, 20 mM imidazole, 20 mM taurine, 50 mM MES hydrate, 0.5 mM DTT, 6.56 mM $MgCl_2$, 5.77 mM ATP and 15 mM phosphocreatine (Doerrier et al., 2018). Diagnostic eosin-hematoxylin (H&E) and basal cell marker p63/tumor cell marker AMACR double-immunostaining (IHC) was performed for each biopsy and the respective surrounding area according to standard procedures for confirmation of tissue identity (Fig. 2). Detailed IHC procedures and antibodies used have been described previously (Schaefer et al., 2013). Clinical characteristics of samples used for the study are included in Table 1.

High-Resolution Respirometry (HRR)

Mechanical permeabilization of the tissue samples was performed in a small glass petri dish on a pre-chilled metal plate in MiR05 + creatine (3 mg/mL; MiR05Cr) buffer with two pairs of sharp forceps for 5 min as reported previously (Schopf et al., 2016). Each permeabilized tissue sample was divided into two smaller samples of equal size, rinsed with ice-cold MiR05Cr, briefly blotted on a filter paper before wet tissue mass was determined. Following permeabilization, each tissue sample was placed into a pre-calibrated chamber of an Oxygraph-2k (O2k, Oroboros Instruments, Innsbruck, Austria). Benign and malignant biopsies were analyzed simultaneously (duplicate measurements in four chambers). All experiments were performed at 37 °C under constant stirring while oxygen concentration was kept between 200 – 300 µM. For real-time data acquisition and post-experimental analysis, DatLab software (Oroboros Instruments, Innsbruck, Austria) was used. Substrate concentrations, their primary sites of action and the corresponding coupling/pathway control states have been described

and are summarized in SI Tables S1 and S2 (Gnaiger, 2009; Gnaiger et al. 2019). Respiratory capacities were expressed as oxygen consumption per wet mass of tissue [pmol s^{-1} mg^{-1}] and corrected for residual oxygen consumption (ROX), measured after inhibition of Complexes CI, CII and CIII. For determination of relative respiratory capacities (flux control ratio, *FCR*) respiratory capacities were normalized to the internal reference state NS_E.

We applied a SUIT protocol to evaluate the activity of different segments of the electron transfer system in three distinct coupling/pathway control states, LEAK, OXPHOS and ET. LEAK respiration was measured in the presence of NADH-linked substrates glutamate (10 mM) and malate (2 mM) (GM), which transfer electrons along CI into the Q-pool. For the determination of corresponding OXPHOS capacity, ADP (2.5 mM) was added at saturating concentrations. This was followed by incubation with H_2O_2 (500 µM) for 15 minutes to induce oxidative stress and assess the effect of damage mediated by elevated cellular ROS levels (Stadlmann et al., 2002). Excess H_2O_2 was then removed by addition of catalase (280 U/mL) and the chambers were briefly opened to regain initial O_2 concentrations. After titration of pyruvate (P, 5 mM), succinate (S,10 mM) was added to fuel electrons via CII, thus reconstituting TCA cycle function and inducing convergent NADH- and succinate-linked (NS) electron flow through CI and CII into the Q-cycle. Subsequently uncoupling was performed by a stepwise titration of uncoupler carbonyl cyanide *p*-trifluoro-methoxyphenyl hydrazone (FCCP, 0.5 µM), which enabled determination of maximal NS-mediated ET-respiratory capacity. Inhibition of CI by rotenone (0.5 µM) revealed S-pathway ET-respiratory capacity. Residual oxygen consumption (*Rox*) was measured after additional inhibition of CII and CIII by malonate (Mna) and antimycin A (Ama), respectively. In control experiments assessing the effect of simulated oxidative stress by H_2O_2 exposure, tissue samples were split, one half was analyzed using the H_2O_2 treatment step, while the other half was incubated with H_2O as a control. In addition, a series of paired BE/CA tissue samples was measured using a protocol omitting the H_2O_2 treatment. The impact of oxidative stress treatment on the single enzymatic step of Complex IV was assessed in split BE tissue samples using a protocol including inhibition of CI, CII and CIII with rotenone, malonate and antimycin A. Ascorbate was added followed by *N,N,N′,N′*-Tetramethyl-1,4-phenylendiamine (TMPD). Chemical background oxygen consumption was measured after inhibition of CIV with sodium azide and was used for correction (SI Table S1,S2; Gnaiger & Kuznetsov 2002).

Next-generation sequencing of the entire mitochondrial genome

After the HRR experiments tissue biopsies were recovered, washed two times with pre-chilled PBS and stored at -80°C until isolation of DNA. Total genomic DNA was extracted using the EZ1 DNA Tissue Kit (Qiagen, Hilden, Germany) following the manufacturers' instructions. The whole mitochondrial genome was amplified in two overlapping PCR fragments of app. 8.5 kbp using the primers 5′-AAATCTTACCCCGCCTGTTT-3′ (fragment A, forward), 5′-AATTAGGCTGTGGGTGGTTG-3′ (fragment A, reverse), 5′- GGCAGGTCAATTTCACTGGT-3′ (fragment B, forward), 5′- GCCATACTAGTCTTTGCCGC-3′ (fragment B, reverse) as reported (Kloss-Brandstatter et al., 2010; Kloss-Brandstatter et al., 2015). After PCR, all amplicons were quality checked after purification on a Fragment Analyzer system using the DNF-930 dsDNA Reagent Kit (Advanced Analytical, Ames, USA).

For generation of barcoded 200 bp insert Ion Torrent NGS libraries, 1 ng of DNA of a 1:1 mixture of both mtDNA fragments A and B was enzymatically fragmented using the NEBNext dsDNA Fragmentase Kit (New England Biolabs, Ipswich, USA), end-repaired with the NEBNext End Repair Module (New England Biolabs) and ligated with IonXpress adapters (Life Technologies, Waltham, MA) using T4 DNA Ligase and Bst DNA Polymerase (New England Biolabs). The ligation products were size selected on a E-Gel SizeSelect Agarose Gel, and amplified using the NEBNext High-Fidelity Kit (New England Biolabs). All post-reaction purification steps were conducted using MagSi-NGS^{PREP} magnetic beads (Magna Medics Diagnostics, Geleen, NL). Size distribution of the enriched libraries was assessed on a Fragment Analyzer system (Advanced Analytical, Ames, USA) while the concentration was determined on a 7900HT Fast Real-Time PCR System. Template positive Ion Sphere Particle (ISP) generation and enrichment, followed by automated chip loading were performed on the Ion Chef System (Life Technologies) using the Ion PI IC 200 Kit. Sequencing on the Ion Proton Sequencer was performed using Ion PI Chips and Ion PI Sequencing 200 Kit v2 chemistry.

Each run included artificial control NGS libraries prepared by mixing the mtDNA of two individuals in a 1+9, 1+49 and 1+99 ratio to generate libraries with known and well-defined HP levels. Each library was sequenced twice via a total of 3 different runs on 3 different plates on the Ion Torrent Proton, comprising controls (such as predefined sample mixtures of 2 previously known haplotypes, and internal control samples). Subsequently the data were joined, by only considering heteroplasmic and homoplasmic variants occurring in data sets. Concordance between the sequencing runs was confirmed by an analysis of the detected variants via the Bland-Altmann method (Fig. 3).

Analysis of mitochondrial DNA next-generation sequencing data

mtDNA data obtained from the Proton sequencer were analyzed using an in-house installation of our previously developed mtDNA-Server based on Cloudgene (Weissensteiner et al., 2016). Sequence reads were aligned to the revised Cambridge Reference Sequence (rCRS) with a distributed version of BWA MEM 7.5 based on JBWA. Haplogroups were determined via HaploGrep (Weissensteiner et al., 2016) to exclude potential sample contaminations. The data was processed with the following parameters: Phred score per base filtering was set to Q20 (1% error rate), alignment score of Q30, mapping Quality Score 20, and the per base alignment quality (BAQ) filtering was applied by adapting GATKs implementation of BAQ for circular genomes. Only HPs exceeding a 2% threshold were accepted for analysis in order to avoid false positive results. This threshold was determined based on the precision and recall accuracy of the four control samples (1+1, 1+9, 1+49 and 1+99 mixtures of two individuals (Weissensteiner et al., 2016). A minimal coverage per strand of >10 bases was considered, while a minimal coverage of 5 bases per strand was required for detection of heteroplasmy variants. Forward and reverse strand were required to show similar results, verified by the strand bias. Private mutations were defined as HPs found in one tissue type only, be it cancer or benign, as opposed to shared HPs present in both tissue types. All found HPs are listed in SI Table S3, categorized in “private benign”, “private cancer” and “shared” HPs.

Prediction of likely pathogenic effects of mt-variants on protein function

To compare mutation profiles in the benign-cancer tissue pairs, variants where classified into three categories: benign variants only, shared variants (assumed as germline variants) and tumor variants only. The variants were subsequently annotated with the pre-computed MutPred scores as provided by Pereira et al in Table S3 of their article (Pereira et al., 2011) and the pre-computed pathogenicity predictions provided by MitImpact 2 (Castellana et al., 2016; Castellana et al., 2017), by downloading the data as tab-delimited file and merging in a relational database.

Mitochondrial Complex I protein structure modelling

Protein structures were inspected and analysed using COOT 0.8.7.1 (Emsley et al., 2010). Mutations were placed using the mutation function in COOT. The ND domains of *Thermus thermophilus* CI crystal structure (PDB: 4HE8 and 4HEA) (Baradaran et al., 2013) were superimposed with the cryo-EM model of the CI subunit of the human respiratory megacomplex (PDB: 5XTD and 5XTC) (Guo et al., 2017) in COOT in order to relate functional details described for *T. thermophilus* to the human cryo-EM structure of CI. Structure figures were generated and rendered with the Chimera 1.1.2 (Goddard et al., 2018). A supplemental iSee package (Raush et al., 2009) has been produced to visualize and examine the functionally relevant mutation sites and can be viewed online in any JavaScript enabled web browser (http://www.ruppweb.org/ICM/).

mtDNA copy number determination

Starting from tissue total DNA extracts mtDNA copy numbers (mt-CN) were determined via duplex qPCR by simultaneous quantification of a mitochondrial (*MT-TL1*) and a nuclear (*B2M*) amplicon on a Quantstudio 6 instrument (Life Technologies) as we reported previously (Bai and Wong, 2005). For improving assay accuracy and minimizing inter-assay variability a plasmid construct containing the MT-TL1 and the B2M amplicons was included as a reference

standard (Fazzini et al., 2018). mt-CN per diploid cell was calculated according to the formula $CN = 2 \times E^{-\Delta\Delta Cq}$, where "ΔΔCq" denotes $(Cq_{mt} - Cq_n)_{sample} - (Cq_{mt} - Cq_n)_{plasmid}$, allowing for the plasmid-based correction.

Global transcriptome next-generation sequencing

Global gene expression analysis was performed by RNA NGS-sequencing. RNA was isolated from frozen tissue blocks from areas surrounding the tissue samples extracted for HRR/mtDNA sequencing (Fig. 1A). Libraries were prepared using the Illumina TruSeq Stranded mRNA LT Sample Preparation Kit and paired-end sequencing was performed on an Illumina HiSeq 2500 instrument (Illumina, San Diego, CA) according to the manufacturer's instruction. The mean relative GM-pathway capacity for all malignant samples in this study was 0.27±0.10 as determined by HRR. Therefore, a GM- pathway contribution of ≤27% relative to maximal OXPHOS capacity was considered as "low" whereas a relative GM-pathway contribution of >27% was considered as "high" GM-pathway capacity.

RNA expression analyses

As a first step before raw sequence data analyses, the *FastQC* tool was applied as quality control (QC) on the sequencing reads from all datasets. The sequencing reads were aligned to the human genome (GRCh38/hg38 assembly) using STAR and processed with *Samtools (Dobin et al., 2013; Li et al., 2009)*. Gene-level read counts were obtained with *htseq-count* of the Python package *HTSeq*, using the default union-counting mode (Anders et al., 2015). The differential gene expression analysis of tumor and non-malignant benign samples was calculated utilizing the *DESeq2* package in R (Love et al., 2014). Clustering and visualization were done with the software Genesis (Sturn et al., 2002). A collection of 1158 human mitochondrial genes for expression analysis was retrieved from MitoCarta2.0 databases.

Metabolic pathway assignment

For pathway analysis and annotation the InnateDB Pathway Analysis online tool was used (http://www.innatedb.ca/redirect.do?go=batchPw) (Breuer et al., 2013). Overexpressed mitochondrial genes based on MitoCarta2.0 database (Calvo et al., 2016) as identified by the RNA-Seq analysis were used to perform a Pathway Over-Representation Analysis (ORA). The KEGG DAVID analysis list restricted to the proteins and enzymes listed in the MitoCarta2 list was used to group the differentially expressed mt-related genes into respective pathways. To test for significant differences in gene expression between benign/malignant and mild/severe phenotype samples, a pairwise comparison between groups for each gene listed in the MitoCarta2 catalogue was performed based on the FPKM values. To control for type-I error accumulation, *p*-values were corrected by the Benjamini–Hochberg procedure.

Extraction of severe respiratory phenotype metagenes and survival analyses

For the identification of a set of differentially expressed genes representative for the severe (low GM) mitochondrial respiratory phenotype ("metagenes"), we selected only significantly correlated genes with an average correlation $r>0.4$ ($p<0.05$) as proposed previously (Angelova et al., 2015). We thus tried to avoid that their correlation might be due to chance while preserving a reasonable number of genes for the severe phenotype metagene set. Clinical variables including disease-free survival (time to biochemical tumor recurrence) and the corresponding RNA-seq expression profiles of prostate adenocarcinoma (PRAD) patients listed in the Cancer Genome Atlas (TCGA) database were downloaded directly from the TCGA Data Portal (https://cancergenome.nih.gov/cancersselected/prostatecancer). For the confirmatory meta-analysis, available clinical data and microarray expression profiles from four additional prostate cancer cohort studies were downloaded from the Gene Expression Omnibus (https://www.ncbi.nlm.nih.gov/geo/): GSE16560 (Human 6k Transcriptionally Informative Gene Panel for DASL; *N*=281) (Sboner et al., 2010), GSE40272 (SMD Print_1529 Homo sapiens; *N*=84) (Gulzar et al., 2013), GSE46602 (Affymetrix GeneChip Human Genome U133 Plus 2.0; *N*=36) (Mortensen et al., 2015), GSE70768 (Illumina HumanHT-12 V4.0

expression beadchip; *N*=111) (Ross-Adams et al., 2015) and GSE70769 (Illumina HumanHT-12 V4.0 expression beadchip; *N*=94) (Ross-Adams et al., 2015). The disease-free survival information for each patient was extracted from the clinical XML files in the complete clinical sets.

Statistical analyses

All statistical analyses were performed using IBM SPSS or R software version 2.0 and numerical data are presented as mean ± SD unless otherwise stated. Normality tests were performed using the Shapiro-Wilk Test followed by Q-Q Plot and histogram evaluation. Accordingly, either Student's paired-samples t-test or Wilcoxon signed rank test was used for group comparisons whereas Wilcoxon rank-sum test and students t-test was used to compare variables among unpaired samples. If multiple paired t-tests were performed on the same sample set, results were corrected according to the Bonferroni-Holm method. For multiple comparisons, one-way analysis of variance (ANOVA) followed by Tukey's honest significant difference test was used. Linear regression models followed by one-way ANOVA were used to test for relationships between independent variables. A multivariate logistic regression analysis was performed to evaluate the relationship between several independent variables (patient age, free PSA ratio and tumor stage) and the presence or absence of heteroplasmies as the dependent variable. Spearman's rank correlation coefficients were calculated to evaluate the presence of significant correlations among non-parametric variables and to test for multicollinearity among single independent variables used in the logistic regression model. The significant differential expression of genes was determined using a false discovery rate (*FDR*) below 0.01 as determined by the Benjamini–Hochberg procedure to control for type-I errors after multiple testing. To test associations between categorical variables either Pearson's Chi-squared test or Fisher's exact test was used. The overall survival time was defined using the latest information. For survival analysis, the patients were dichotomized based on the expression levels of the low-GM metagenes. The optimal cutpoints were searched within the inner 80% selection interval and chosen based on a minimal corrected *p*-value as proposed previously (Altman et al., 1994) and based on a maximum Harrell's C indices (Harrell, Jr. et al., 1996). Disease-free survival (DFS) probability curves were calculated via the Kaplan-Meier method while differences in disease outcome were analyzed using Hazard ratios and stratified log-rank test. Univariate and multivariate Cox regression analysis on DFS was performed using age, Gleason score, TNM staging and total serum PSA values as binary covariates, for all cohorts mentioned above. For all analyses, IBM SPSS or R software version 2.0 including the *survival* package were used. Statistically significant differences are denoted *, $p<0.05$; **, $p<0.01$; ***, $p<0.001$; $p\leq0.05$ was considered not statistically significant.

Data availability

Detailed sample and clinical data (“Sample&ClinicalData”), detailed information on mtDNA sequencing and details of all heteroplasmies detected (“mtDNA_HeteroplasmieData”), RNAseq gene expression data (“Normalized_RNAseqExpressionData”) and mtDNAseq and RNAseq raw data will be made available upon acceptance of the manuscript on the European Genomics Archive platform, EGA (https://ega-archive.org).

Acknowledgements

The study was funded within the COMET K1 Center Oncotyrol - Center for Personalized Medicine by the Austrian Research Promotion Agency (FFG) and the Tyrolean Future Foundation, and the K-Regio project MitoFit funded by the Tyrolian Government, a contribution to COST Action MitoEAGLE supported by COST (European Cooperation in Science and Technology).

Competing financial interests

E.G. is founder and CEO of Oroboros Instruments, Innsbruck, Austria.

Author contributions

HK, EG and BS conceived and designed the research; BS, GS, HW, AN, LF, VB, UG, EG, FK, AN and HK planned experiments; BS, GS, AN and FF performed experiments; VB, IE, PS and US performed RNA-seq; AN and BR performed structural analyses; BS, GS, HW, AN, FF, AN, BR, CP, VB, IE, FK and PS analyzed and interpreted data; BS, HW, FF, CP, AN, EG and HK wrote the manuscript; HK organized and supervised the study. All authors reviewed and approved the manuscript for publication.

Abbreviations:

AMACR, alpha-methylacyl-CoA racemase; CDK, cyclin-dependent kinase; CI to CIV, mitochondrial Complexes I to IV; CN, copy number; DSF, disease-free survival; ERG, v-ets avian erythroblastosis virus E26 oncogene related; ET, electron transfer; ETS, electron transfer system; F-ATPase, ATP synthase; FCR, flux control ratio; FDR, false discovery rate; FPKM, fragments per kilobase million; HE, haematoxylin and eosin; HP, heteroplasmy; HRR, high-resolution respirometry; IHC, immunohistochemistry; LEAK respiration, leak compensating respiration in the absence of ATP synthesis; mt, mitochondria or mitochondrial; mtDNA, mitochondrial DNA; nDNA, nuclear DNA; N-pathway capacity, NADH-linked respiratory capacity through CI, CIII and CIV; NGS, next-generation sequencing; OXPHOS, oxidative phosphorylation; PCa, prostate cancer; PSA, prostate-specific antigen; PTEN, Phosphatase and Tensin homolog; ROS, reactive oxygen species; ROX, residual oxygen consumption; S-pathway capacity, succinate-linked respiratory capacity through CII, CIII and CIV; TCA, tricarboxylic-acid cycle; TMPRSS2, transmembrane protease, serine 2.

References

DG Altman, B Lausen, W Sauerbrei, M Schumacher (1994). Dangers of using "optimal" cutpoints in the evaluation of prognostic factors. J.Natl.Cancer Inst., 86, 829-835

S Anders, PT Pyl, W Huber (2015). HTSeq--a Python framework to work with high-throughput sequencing data. *Bioinformatics., 31,* 166-169.btu638 [pii];10.1093/bioinformatics/btu638 [doi]

M Angelova, P Charoentong, H Hackl, ML Fischer, R Snajder, AM Krogsdam, MJ Waldner, G Bindea, B Mlecnik, J Galon, Z Trajanoski (2015). Characterization of the immunophenotypes and antigenomes of colorectal cancers reveals distinct tumor escape mechanisms and novel targets for immunotherapy. *Genome Biol., 16,* 64.s13059-015-0620-6 [pii];10.1186/s13059-015-0620-6 [doi]

RS Arnold, CQ Sun, JC Richards, G Grigoriev, IM Coleman, PS Nelson, CL Hsieh, JK Lee, Z Xu, A Rogatko, AO Osunkoya, M Zayzafoon, L Chung, JA Petros (2009). Mitochondrial DNA mutation stimulates prostate cancer growth in bone stromal environment. *Prostate, 69,* 1-11.10.1002/pros.20854 [doi]

RK Bai , LJ Wong (2005). Simultaneous detection and quantification of mitochondrial DNA deletion(s), depletion, and over-replication in patients with mitochondrial disease. *J.Mol.Diagn., 7,* 613-622.S1525-1578(10)60595-8 [pii];10.1016/S1525-1578(10)60595-8 [doi]

Y Bai, RM Shakeley, G Attardi (2000). Tight control of respiration by NADH dehydrogenase ND5 subunit gene expression in mouse mitochondria. *Mol.Cell Biol., 20,* 805-815

R Baradaran, JM Berrisford, GS Minhas, LA Sazanov (2013). Crystal structure of the entire respiratory complex I. *Nature, 494,* 443-448.nature11871 [pii];10.1038/nature11871 [doi]

MF Berger, MS Lawrence, F Demichelis, Y Drier, K Cibulskis, AY Sivachenko, A Sboner, R Esgueva, D Pflueger, C Sougnez, R Onofrio, SL Carter, K Park, L Habegger, L Ambrogio, T Fennell, M Parkin, G Saksena, D Voet, AH Ramos, TJ Pugh, J Wilkinson, S Fisher, W Winckler, S Mahan, K Ardlie, J Baldwin, JW Simons, N Kitabayashi, TY MacDonald, PW Kantoff, L Chin, SB Gabriel, MB Gerstein, TR Golub, M Meyerson, A Tewari, ES Lander, G Getz, MA Rubin, LA Garraway (2011). The genomic complexity of primary human prostate cancer. *Nature, 470,* 214-220.nature09744 [pii];10.1038/nature09744 [doi]

K Breuer, AK Foroushani, MR Laird, C Chen, A Sribnaia, R Lo, GL Winsor, RE Hancock, FS Brinkman, DJ Lynn (2013). InnateDB: systems biology of innate immunity and beyond--recent updates and continuing curation. *Nucleic Acids Res., 41,* D1228-D1233.gks1147 [pii];10.1093/nar/gks1147 [doi]

SE Calvo, KR Clauser, VK Mootha (2016). MitoCarta2.0: an updated inventory of mammalian mitochondrial proteins. *Nucleic Acids Res., 44,* D1251-D1257.gkv1003 [pii];10.1093/nar/gkv1003 [doi]

S Castellana, C Fusilli, T Mazza (2016). A Broad Overview of Computational Methods for Predicting the Pathophysiological Effects of Non-synonymous Variants. *Methods Mol.Biol., 1415,* 423-440.10.1007/978-1-4939-3572-7_22 [doi]

S Castellana, C Fusilli, G Mazzoccoli, T Biagini, D Capocefalo, M Carella, AL Vescovi, T Mazza (2017). High-confidence assessment of functional impact of human mitochondrial non-synonymous genome variations by APOGEE. *PLoS.Comput.Biol., 13,* e1005628.10.1371/journal.pcbi.1005628 [doi];PCOMPBIOL-D-16-01580 [pii]

CC Cook, A Kim, S Terao, A Gotoh, M Higuchi (2012). Consumption of oxygen: a mitochondrial-generated progression signal of advanced cancer. *Cell Death.Dis., 3,* e258.cddis2011141 [pii];10.1038/cddis.2011.141 [doi]

LC Costello , RB Franklin (2016). A comprehensive review of the role of zinc in normal prostate function and metabolism; and its implications in prostate cancer. *Arch.Biochem.Biophys., 611,* 100-112.S0003-9861(16)30136-9 [pii];10.1016/j.abb.2016.04.014 [doi]

A Dobin, CA Davis, F Schlesinger, J Drenkow, C Zaleski, S Jha, P Batut, M Chaisson, TR Gingeras (2013). STAR: ultrafast universal RNA-seq aligner. *Bioinformatics., 29,* 15-21.bts635 [pii];10.1093/bioinformatics/bts635 [doi]

C Doerrier, Garcia-Souza LF, Krumschnabel G, Wohlfarter Y, Mészáros AT, Gnaiger E (2018) High-Resolution FluoRespirometry and OXPHOS protocols for human cells, permeabilized fibers from small biopsies of muscle, and isolated mitochondria. Methods Mol Biol 1782:31-70.

A Dueregger, B Schopf, T Eder, J Hofer, E Gnaiger, A Aufinger, L Kenner, B Perktold, R Ramoner, H Klocker, IE Eder (2015). Differential Utilization of Dietary Fatty Acids in Benign and Malignant Cells of the Prostate. *PLoS.One., 10,* e0135704.10.1371/journal.pone.0135704 [doi];PONE-D-15-22093 [pii]

P Emsley, B Lohkamp, WG Scott, K Cowtan (2010). Features and development of Coot. Acta Crystallogr.D.Biol.Crystallogr., 66, 486-501.S0907444910007493 [pii];10.1107/S0907444910007493 [doi]

F Fazzini, B Schopf, M Blatzer, S Coassin, AA Hicks, F Kronenberg, L Fendt (2018). Plasmid-normalized quantification of relative mitochondrial DNA copy number. *Sci.Rep., 8,* 15347.10.1038/s41598-018-33684-5 [doi];10.1038/s41598-018-33684-5 [pii]

R Feichtinger, G Schaefer, C Seifarth, JA Mayr, B Kofler, H Klocker (2018). Reduced levels of ATP synthase subunit ATP5F1A correlate with earlier-onset prostate cancer. *Oxid Med Cell Longev, 1347174,*

G Gasparre, I Kurelac, M Capristo, L Iommarini, A Ghelli, C Ceccarelli, G Nicoletti, P Nanni, GC De, K Scotlandi, CM Betts, V Carelli, PL Lollini, G Romeo, M Rugolo, AM Porcelli (2011). A mutation threshold distinguishes the antitumorigenic effects of the mitochondrial gene MTND1, an oncojanus function. *Cancer Res., 71,* 6220-6229.0008-5472.CAN-11-1042 [pii];10.1158/0008-5472.CAN-11-1042 [doi]

E Gnaiger (2009). Capacity of oxidative phosphorylation in human skeletal muscle: new perspectives of mitochondrial physiology. *Int.J.Biochem.Cell Biol., 41,* 1837-1845.S1357-2725(09)00117-4 [pii];10.1016/j.biocel.2009.03.013 [doi]

E Gnaiger, Aasander Frostner E, Abdul Karim N, Abumrad NA, Acuna-Castroviejo D, Adiele RC, et al (2019) Mitochondrial respiratory states and rates. MitoFit Preprint Arch doi:10.26124/mitofit:190001.v4.

TD Goddard, CC Huang, EC Meng, EF Pettersen, GS Couch, JH Morris, TE Ferrin (2018). UCSF ChimeraX: Meeting modern challenges in visualization and analysis. Protein Sci., 27, 14-25.10.1002/pro.3235 [doi]

ZG Gulzar, JK McKenney, JD Brooks (2013). Increased expression of NuSAP in recurrent prostate cancer is mediated by E2F1. *Oncogene, 32,* 70-77.onc201227 [pii];10.1038/onc.2012.27 [doi]

R Guo, S Zong, M Wu, J Gu, M Yang (2017). Architecture of Human Mitochondrial Respiratory Megacomplex I2III2IV2. Cell, 170, 1247-1257.S0092-8674(17)30887-5 [pii];10.1016/j.cell.2017.07.050 [doi]FE Harrell, Jr., KL Lee, DB Mark (1996). Multivariable prognostic models: issues in developing models, evaluating assumptions and adequacy, and measuring and reducing errors. *Stat.Med., 15,* 361-387.10.1002/(SICI)1097-0258(19960229)15:4<361::AID-SIM168>3.0.CO;2-4 [pii];10.1002/(SICI)1097-0258(19960229)15:4<361::AID-SIM168>3.0.CO;2-4 [doi]

JF Hopkins, VY Sabelnykova, J Weischenfeldt, R Simon, JA Aguiar, R Alkallas, LE Heisler, J Zhang, JD Watson, MLK Chua, M Fraser, F Favero, C Lawerenz, C Plass, G Sauter, JD McPherson, T Van Der Kwast, J Korbel, T Schlomm, RG Bristow, PC Boutros (2017). Mitochondrial mutations drive prostate cancer aggression. *Nat.Commun., 8,* 656.10.1038/s41467-017-00377-y [doi];10.1038/s41467-017-00377-y [pii]

SS Hung, NJ Van Bergen, S Jackson, H Liang, DA Mackey, D Hernandez, SY Lim, AW Hewitt, I Trounce, A Pebay, RC Wong (2016). Study of mitochondrial respiratory defects on reprogramming to human induced pluripotent stem cells. *Aging (Albany.NY), 8,* 945-957.100950 [pii];10.18632/aging.100950 [doi]

L Ippolito, A Marini, L Cavallini, A Morandi, L Pietrovito, G Pintus, E Giannoni, T Schrader, M Puhr, P Chiarugi, ML Taddei (2016). Metabolic shift toward oxidative phosphorylation in docetaxel resistant prostate cancer cells. *Oncotarget., 7,* 61890-61904.11301 [pii];10.18632/oncotarget.11301 [doi]

AM James, YH Wei, CY Pang, MP Murphy (1996). Altered mitochondrial function in fibroblasts containing MELAS or MERRF mitochondrial DNA mutations. *Biochem.J., 318 (Pt 2),* 401-407

YS Ju, LB Alexandrov, M Gerstung, I Martincorena, S Nik-Zainal, M Ramakrishna, HR Davies, E Papaemmanuil, G Gundem, A Shlien, N Bolli, S Behjati, PS Tarpey, J Nangalia, CE Massie, AP Butler, JW Teague, GS Vassiliou, AR Green, MQ Du, A Unnikrishnan, JE Pimanda, BT Teh, N Munshi, M Greaves, P Vyas, AK El-Naggar, T Santarius, VP Collins, R Grundy, JA Taylor, DN Hayes, D Malkin, CS Foster, AY Warren, HC Whitaker, D Brewer, R Eeles, C Cooper, D Neal, T Visakorpi, WB Isaacs, GS Bova, AM Flanagan, PA Futreal, AG Lynch, PF Chinnery, U McDermott, MR Stratton, PJ Campbell (2014). Origins and functional consequences of somatic mitochondrial DNA mutations in human cancer. *Elife., 3*.10.7554/eLife.02935 [doi]AMF Kalsbeek, EKF Chan, NM Corcoran, CM Hovens, VM Hayes (2017). Mitochondrial genome variation and prostate cancer: a review of the mutational landscape and application to clinical management. *Oncotarget., 8,* 71342-71357.10.18632/oncotarget.19926 [doi];19926 [pii]

AMF Kalsbeek, EKF Chan, J Grogan, DC Petersen, W Jaratlerdsiri, R Gupta, RJ Lyons, AM Haynes, LG Horvath, JG Kench, PD Stricker, VM Hayes (2018). Altered mitochondrial genome content signals worse pathology and prognosis in prostate cancer. *Prostate, 78,* 25-31.10.1002/pros.23440 [doi]

DM Kirby, A Boneh, CW Chow, A Ohtake, MT Ryan, D Thyagarajan, DR Thorburn (2003). Low mutant load of mitochondrial DNA G13513A mutation can cause Leigh's disease. *Ann.Neurol., 54,* 473-478.10.1002/ana.10687 [doi]

A Kloss-Brandstatter, G Schafer, G Erhart, A Huttenhofer, S Coassin, C Seifarth, M Summerer, J Bektic, H Klocker, F Kronenberg (2010). Somatic mutations throughout the entire mitochondrial genome are associated with elevated PSA levels in prostate cancer patients. *Am.J.Hum.Genet., 87,* 802-812.S0002-9297(10)00588-4 [pii];10.1016/j.ajhg.2010.11.001 [doi]

A Kloss-Brandstatter, H Weissensteiner, G Erhart, G Schafer, L Forer, S Schonherr, D Pacher, C Seifarth, A Stockl, L Fendt, I Sottsas, H Klocker, CW Huck, M Rasse, F Kronenberg, FR Kloss (2015). Validation of Next-Generation Sequencing of Entire Mitochondrial Genomes and the Diversity of Mitochondrial DNA Mutations in Oral Squamous Cell Carcinoma. *PLoS.One., 10,* e0135643.10.1371/journal.pone.0135643 [doi];PONE-D-15-21472 [pii]

K Kluckova, A Bezawork-Geleta, J Rohlena, L Dong, J Neuzil (2013). Mitochondrial complex II, a novel target for anti-cancer agents. *Biochim.Biophys.Acta, 1827,* 552-564.S0005-2728(12)01072-9 [pii];10.1016/j.bbabio.2012.10.015 [doi]

H Li, B Handsaker, A Wysoker, T Fennell, J Ruan, N Homer, G Marth, G Abecasis, R Durbin (2009). The Sequence Alignment/Map format and SAMtools. *Bioinformatics., 25,* 2078-2079.btp352 [pii];10.1093/bioinformatics/btp352 [doi]

J Lindberg, IG Mills, D Klevebring, W Liu, M Neiman, J Xu, P Wikstrom, P Wiklund, F Wiklund, L Egevad, H Gronberg (2013). The mitochondrial and autosomal mutation landscapes of prostate cancer. *Eur.Urol., 63,* 702-708.S0302-2838(12)01438-8 [pii];10.1016/j.eururo.2012.11.053 [doi]

MI Love, W Huber, S Anders (2014). Moderated estimation of fold change and dispersion for RNA-seq data with DESeq2. *Genome Biol., 15,* 550.s13059-014-0550-8 [pii];10.1186/s13059-014-0550-8 [doi]

M Malvezzi, P Bertuccio, T Rosso, M Rota, F Levi, VC La, E Negri (2015). European cancer mortality predictions for the year 2015: does lung cancer have the highest death rate in EU women? *Ann.Oncol., 26,* 779-786.mdv001 [pii];10.1093/annonc/mdv001 [doi]

JA Mayr, D Meierhofer, F Zimmermann, R Feichtinger, C Kogler, M Ratschek, N Schmeller, W Sperl, B Kofler (2008). Loss of complex I due to mitochondrial DNA mutations in renal oncocytoma. *Clin.Cancer Res., 14,* 2270-2275.14/8/2270 [pii];10.1158/1078-0432.CCR-07-4131 [doi]

JP Mazat, T Letellier, F Bedes, M Malgat, B Korzeniewski, LS Jouaville, R Morkuniene (1997). Metabolic control analysis and threshold effect in oxidative phosphorylation: implications for mitochondrial pathologies. *Mol.Cell Biochem., 174,* 143-148

JP Mazat, R Rossignol, M Malgat, C Rocher, B Faustin, T Letellier (2001). What do mitochondrial diseases teach us about normal mitochondrial functions.that we already knew: threshold expression of mitochondrial defects. *Biochim.Biophys.Acta, 1504,* 20-30.S0005-2728(00)00236-X [pii]

R McFarland, DM Kirby, KJ Fowler, A Ohtake, MT Ryan, DJ Amor, JM Fletcher, JW Dixon, FA Collins, DM Turnbull, RW Taylor, DR Thorburn (2004). De novo mutations in the mitochondrial ND3 gene as a cause of infantile mitochondrial encephalopathy and complex I deficiency. *Ann.Neurol., 55,* 58-64.10.1002/ana.10787 [doi]

A Moore, Q Lan, JN Hofmann, CS Liu, WL Cheng, TT Lin, SI Berndt (2017). A prospective study of mitochondrial DNA copy number and the risk of prostate cancer. *Cancer Causes Control, 28,* 529-538.10.1007/s10552-017-0879-x [doi];10.1007/s10552-017-0879-x [pii]

M Mort, US Evani, VG Krishnan, KK Kamati, PH Baenziger, A Bagchi, BJ Peters, R Sathyesh, B Li, Y Sun, B Xue, NH Shah, MG Kann, DN Cooper, P Radivojac, SD Mooney (2010). In silico functional

profiling of human disease-associated and polymorphic amino acid substitutions. *Hum.Mutat., 31,* 335-346.10.1002/humu.21192 [doi]

MM Mortensen, S Hoyer, AS Lynnerup, TF Orntoft, KD Sorensen, M Borre, L Dyrskjot (2015). Expression profiling of prostate cancer tissue delineates genes associated with recurrence after prostatectomy. *Sci.Rep., 5,* 16018.srep16018 [pii];10.1038/srep16018 [doi]

JR Packer , NJ Maitland (2016). The molecular and cellular origin of human prostate cancer. *Biochim.Biophys.Acta, 1863,* 1238-1260.S0167-4889(16)30041-6 [pii];10.1016/j.bbamcr.2016.02.016 [doi]

S Paglialunga, BB van, M Bosma, MP Valdecantos, E Amengual-Cladera, JA Jorgensen, BD van, GJM den Hartog, DM Ouwens, JJ Briede, P Schrauwen, J Hoeks (2012). Targeting of mitochondrial reactive oxygen species production does not avert lipid-induced insulin resistance in muscle tissue from mice. *Diabetologia, 55,* 2759-2768.10.1007/s00125-012-2626-x [doi];10.1007/s00125-012-2626-x [pii]

JS Park, LK Sharma, H Li, R Xiang, D Holstein, J Wu, J Lechleiter, SL Naylor, JJ Deng, J Lu, Y Bai (2009). A heteroplasmic, not homoplasmic, mitochondrial DNA mutation promotes tumorigenesis via alteration in reactive oxygen species generation and apoptosis. *Hum.Mol.Genet., 18,* 1578-1589.ddp069 [pii];10.1093/hmg/ddp069 [doi]

NN Pavlova , CB Thompson (2016). The Emerging Hallmarks of Cancer Metabolism. *Cell Metab, 23,* 27-47.S1550-4131(15)00621-X [pii];10.1016/j.cmet.2015.12.006 [doi]

L Pereira, P Soares, P Radivojac, B Li, DC Samuels (2011). Comparing phylogeny and the predicted pathogenicity of protein variations reveals equal purifying selection across the global human mtDNA diversity. *Am.J.Hum.Genet., 88,* 433-439.S0002-9297(11)00098-X [pii];10.1016/j.ajhg.2011.03.006 [doi]

JA Petros, AK Baumann, E Ruiz-Pesini, MB Amin, CQ Sun, J Hall, S Lim, MM Issa, WD Flanders, SH Hosseini, FF Marshall, DC Wallace (2005). mtDNA mutations increase tumorigenicity in prostate cancer. *Proc.Natl.Acad.Sci.U.S.A, 102,* 719-724.0408894102 [pii];10.1073/pnas.0408894102 [doi]

M Picard, J Zhang, S Hancock, O Derbeneva, R Golhar, P Golik, S O'Hearn, S Levy, P Potluri, M Lvova, A Davila, CS Lin, JC Perin, EF Rappaport, H Hakonarson, IA Trounce, V Procaccio, DC Wallace (2014). Progressive increase in mtDNA 3243A>G heteroplasmy causes abrupt transcriptional reprogramming. *Proc.Natl.Acad.Sci.U.S.A, 111,* E4033-E4042.1414028111 [pii];10.1073/pnas.1414028111 [doi]

CL Quinlan, JR Treberg, IV Perevoshchikova, AL Orr, MD Brand (2012). Native rates of superoxide production from multiple sites in isolated mitochondria measured using endogenous reporters. *Free Radic.Biol.Med., 53,* 1807-1817.S0891-5849(12)00504-7 [pii];10.1016/j.freeradbiomed.2012.08.015 [doi]

E Raush, M Totrov, BD Marsden, R Abagyan (2009). A new method for publishing three-dimensional content. PLoS.One., 4, e7394.10.1371/journal.pone.0007394 [doi]

H Ross-Adams, AD Lamb, MJ Dunning, S Halim, J Lindberg, CM Massie, LA Egevad, R Russell, A Ramos-Montoya, SL Vowler, NL Sharma, J Kay, H Whitaker, J Clark, R Hurst, VJ Gnanapragasam, NC Shah, AY Warren, CS Cooper, AG Lynch, R Stark, IG Mills, H Gronberg, DE Neal (2015). Integration of copy number and transcriptomics provides risk stratification in prostate cancer: A discovery and validation cohort study. *EBioMedicine., 2,* 1133-1144.10.1016/j.ebiom.2015.07.017 [doi];S2352-3964(15)30071-2 [pii]

R Rossignol, B Faustin, C Rocher, M Malgat, JP Mazat, T Letellier (2003). Mitochondrial threshold effects. *Biochem.J., 370,* 751-762.10.1042/BJ20021594 [doi];BJ20021594 [pii]

A Sboner, F Demichelis, S Calza, Y Pawitan, SR Setlur, Y Hoshida, S Perner, HO Adami, K Fall, LA Mucci, PW Kantoff, M Stampfer, SO Andersson, E Varenhorst, JE Johansson, MB Gerstein, TR Golub, MA Rubin, O Andren (2010). Molecular sampling of prostate cancer: a dilemma for predicting disease progression. *BMC.Med.Genomics, 3,* 8.1755-8794-3-8 [pii];10.1186/1755-8794-3-8 [doi]

G Schaefer, JM Mosquera, R Ramoner, K Park, A Romanel, E Steiner, W Horninger, J Bektic, M Ladurner-Rennau, MA Rubin, F Demichelis, H Klocker (2013). Distinct ERG rearrangement prevalence in prostate cancer: higher frequency in young age and in low PSA prostate cancer. *Prostate Cancer Prostatic.Dis., 16,* 132-138.pcan20134 [pii];10.1038/pcan.2013.4 [doi]

B Schopf, G Schafer, A Weber, H Talasz, IE Eder, H Klocker, E Gnaiger (2016). Oxidative phosphorylation and mitochondrial function differ between human prostate tissue and cultured cells. *FEBS J., 283,* 2181-2196.10.1111/febs.13733 [doi]

W Sperl, D Skladal, E Gnaiger, M Wyss, U Mayr, J Hager, FN Gellerich (1997). High resolution respirometry of permeabilized skeletal muscle fibers in the diagnosis of neuromuscular disorders. *Mol.Cell Biochem., 174,* 71-78

S Stadlmann, G Rieger, A Amberger, AV Kuznetsov, R Margreiter, E Gnaiger (2002). H_2O_2-mediated oxidative stress versus cold ischemia-reperfusion: mitochondrial respiratory defects in cultured human endothelial cells. *Transplantation, 74,* 1800-1803.10.1097/01.TP.0000039262.25355.67 [doi]

UH Stenman, PA Abrahamsson, G Aus, H Lilja, C Bangma, FC Hamdy, L Boccon-Gibod, P Ekman (2005). Prognostic value of serum markers for prostate cancer. *Scand.J.Urol.Nephrol.Suppl,* 64-81. W2451251K65672K1 [pii];10.1080/03008880510030941 [doi]

A Sturn, J Quackenbush, Z Trajanoski (2002). Genesis: cluster analysis of microarray data. *Bioinformatics., 18,* 207-208

L Tretter, A Patocs, C Chinopoulos (2016). Succinate, an intermediate in metabolism, signal transduction, ROS, hypoxia, and tumorigenesis. *Biochim.Biophys.Acta, 1857,* 1086-1101.S0005-2728(16)30059-7 [pii];10.1016/j.bbabio.2016.03.012 [doi]

L Valcarcel-Jimenez, E Gaude, V Torrano, C Frezza, A Carracedo (2017). Mitochondrial Metabolism: Yin and Yang for Tumor Progression. *Trends Endocrinol.Metab, 28,* 748-757.S1043-2760(17)30087-5 [pii];10.1016/j.tem.2017.06.004 [doi]

L Valente, D Piga, E Lamantea, F Carrara, G Uziel, P Cudia, A Zani, L Farina, L Morandi, M Mora, A Spinazzola, M Zeviani, V Tiranti (2009). Identification of novel mutations in five patients with mitochondrial encephalomyopathy. *Biochim.Biophys.Acta, 1787,* 491-501.S0005-2728(08)00691-9 [pii];10.1016/j.bbabio.2008.10.001 [doi]

T Wai, D Teoli, EA Shoubridge (2008). The mitochondrial DNA genetic bottleneck results from replication of a subpopulation of genomes. *Nat.Genet., 40,* 1484-1488.ng.258 [pii];10.1038/ng.258 [doi]

A Weber, H Klocker, H Oberacher, E Gnaiger, H Neuwirt, N Sampson, IE Eder (2018). Succinate Accumulation Is Associated with a Shift of Mitochondrial Respiratory Control and HIF-1alpha Upregulation in PTEN Negative Prostate Cancer Cells. *Int.J.Mol.Sci., 19*.ijms19072129 [pii];10.3390/ijms19072129 [doi]

H Weissensteiner, L Forer, C Fuchsberger, B Schopf, A Kloss-Brandstatter, G Specht, F Kronenberg, S Schonherr (2016). mtDNA-Server: next-generation sequencing data analysis of human mitochondrial DNA in the cloud. *Nucleic Acids Res., 44,* W64-W69.gkw247 [pii];10.1093/nar/gkw247 [doi]

H Weissensteiner, D Pacher, A Kloss-Brandstatter, L Forer, G Specht, HJ Bandelt, F Kronenberg, A Salas, S Schonherr (2016). HaploGrep 2: mitochondrial haplogroup classification in the era of high-throughput sequencing. *Nucleic Acids Res., 44,* W58-W63.gkw233 [pii];10.1093/nar/gkw233 [doi]

LJ Wong, MH Liang, H Kwon, RK Bai, O Alper, A Gropman (2002). A cystic fibrosis patient with two novel mutations in mitochondrial DNA: mild disease led to delayed diagnosis of both disorders. *Am.J.Med Genet., 113,* 59-64.10.1002/ajmg.10767 [doi]

Supplemantary tables

Table S1: Respiratory states and flux control ratios.

The substrate-uncoupler-inhibitor titration protocol (SUIT, http://www.mitofit.org/index.php/SUIT-014) provides a sequential analysis of mitochondrial respiratory capacity in electron transfer-pathway states and specific respiratory coupling control states

Step: Metabolic control variable	Abbreviation concentration	Pathway (Q-junction)	Respiratory state	Ref. State SUIT protocol	Flux control ratio, *FCR*	Significance
1: glutamate & malate	G 10 mM & M 2 mM	N (CI)	GM_L	NS_E	GM_L/NS_E	N-pathway (GM), LEAK respiration
2: ADP H_2O_2, oxid. Stress	D 2.5 mM 0.5 mM (15 min)	N (CI)	$GM_{P,pre}$ GM_P	NS_E NS_E	GM_L/NS_E $GM_{P,pre}/NS_E$	N-pathway (GM), OXPHOS capacity GM_P inhibited by oxidative stress
3: pyruvate	P 5 mM	N (CI)	$N(PGM)_P$; N_P	NS_E	GM_P/NS_E	N-pathway (PGM), OXPHOS capacity
4: succinate	S 10 mM	NS (CI&II)	NS_P	NS_E	N_P/NS_E	NS-pathway (PGMS), OXPHOS capacity
5: uncoupler (FCCP)	U 0.5 µM steps	NS (CI&II)	NS_E	NS_E	NS_P/NS_E	NS-pathway (PGMS), ET capacity
6: rotenone	Rot 0.5 µM	S (CII)	S_E	NS_E	S_E/NS_E	S-pathway (S), inhibition CI; ET capacity
7: malonate & antimycin A	Mna 5 mM & Ama 2.5 µM		ROX	NS_E+*Rox*	*Rox*/(NS_{E+Rox})	inhibition CII inhibition CIII; residual O_2 consumption
8: ascorbate & TMPD	As 2 mM & Tm 0.5 mM		CIV	NS_E	CIV/NS_E	single step CIV activity
9: azide	Azd 100 mM		chem. background			inhibition CIV; autoxidation of As&Tm

Table S2: Effect of metabolic control variables on mitochondrial respiratory capacities.

Step: Metabolic control variable	Background state	Ref. state Single step	Flux control ratio, *FCR*	Difference of flux [pmol s^{-1} mg^{-1}]	Significance
1: glutamate & malate	ROX	GM_L			GM-pathway, LEAK respiration
2: ADP H_2O_2, oxid. stress	GM_L $GM_{P,pre}$	$GM_{P,pre}$ GM_P	$GM_L/GM_{P,pre}$ $GM_{P,pre}/GM_P$	$GM_{P,pre}$-GM_L GM_P-$GM_{P,pre}$	OXPHOS efficiency inhibition by oxidative stress
3: pyruvate	GM_P	N_P	GM_P/N_P	N_P-GM_P	stimulation by P in CI-convergent N-pathways
4: succinate	N_P	NS_P	N_P/NS_P	NS_P-N_P	stimulation by S in CI&II-convergent NS-pathways
5: uncoupler	NS_P	NS_E	NS_P/NS_E	NS_E-NS_P	*E-P* excess capacity
6: rotenone (inhibition CI)	S_E	NS_E	S_E/NS_E	NS_E-S_E	stimulation by PGM in CI&II-convergent NS-pathways

Table S3. mtDNA heteroplasmies.

Heteroplasmy variants exhibiting a heteroplasmy level >2%. Locations, heteroplasmy variants, gene location, heteroplasmy level, report status (0=not reported and 1=previously reported) and amino acid substitution caused by the heteroplasmies found in either both tissues (shared heteroplasmies), only the benign (private benign heteroplasmies) or only the malignant (private cancer heteroplasmies) tissues.

Position	Sample	Tissue	Heteroplasmy	Gene	HP level %	Reported*	Amino acid subst
Heteroplasmies found in benign and malignant tissue samples (shared heteroplasmies)							
72	PK_62	BE	T-C	DLOOP2	98	1	non-coding
72		CA			97		
119	PK_79	BE	T-C	DLOOP2	96	1	non-coding
119		CA			97		
146	PK_93	BE	T-C	DLOOP2	2	1	non-coding
146		CA			3		
185	PK_66	BE	G-A	DLOOP2	97	1	non-coding
185		CA			98		
189	PK_47	BE	A-G	DLOOP2	97	1	non-coding
189		CA			55		
194	PK_72	BE	C-T	DLOOP2	91	1	non-coding
194		CA			90		
194	PK_79	BE	C-T	DLOOP2	90	1	non-coding
194		CA			93		
194	PK_97	BE	C-T	DLOOP2	93	1	non-coding
194		CA			94		
195	PK_97	BE	T-C	DLOOP2	95	1	non-coding
195		CA			97		
200	PK_74	BE	A-G	DLOOP2	94	1	non-coding
200		CA			96		
204	PK_41	BE	T-C	DLOOP2	10	1	non-coding
204		CA			11		
1284	PK_90	BE	T-C	RNR1	73	1	non-coding
1284		CA			74		
6040	PK_73	BE	A-G	CO1	14	1	N46S
6040		CA			10		
6519	PK_98	BE	A-G	CO1	12	0	I206V
6519		CA			4		
11252	PK_32	BE	A-G	ND4	7	1	I165V
11252		CA			4		
13590	PK_57	BE	G-A	ND5	14	1	syn
13590		CA			6		
13755	PK_87	BE	C-T	ND5	16	1	syn
13755		CA			4		
15005	PK_57	BE	G-A	CYB	6	0	A87T
15005		CA			2		
15140	PK_33	BE	G-A	CYB	11	0	V132I
15140		CA			3		
15242	PK_72	BE	G-A	CYB	10	0	syn
15242		CA			12		
15265	PK_87	BE	C-G	CYB	17	0	syn
15265		CA			5		
16093	PK_40	BE	T-C	DLOOP1	66	1	non-coding
16093		CA			79		
16093	PK_60	BE	T-C	DLOOP1	56	1	non-coding
16093		CA			94		

16192 16192	PK_67	BE CA	C-T	DLOOP1	97 97	1	non-coding
16192 16192	PK_75	BE CA	C-T	DLOOP1	95 94	1	non-coding
16192 16192	PK_79	BE CA	C-T	DLOOP1	92 97	1	non-coding
16192 16192	PK_81	BE CA	C-T	DLOOP1	95 96	1	non-coding
16192 16192	PK_94	BE CA	C-T	DLOOP1	96 97	1	non-coding
16192 16192	PK_97	BE CA	C-T	DLOOP1	94 95	1	non-coding
16216 16216	PK_90	BE CA	A-C	DLOOP1	11 8	0	non-coding

Heteroplasmies found only in benign tissue samples (private benign heteroplasmies)

72	PK_68	BE	T-C	DLOOP2	2	1	non-coding
72	PK_30	BE	T-C	DLOOP2	4	1	non-coding
152	PK_72	BE	T-C	DLOOP2	2	1	non-coding
185	PK_90	BE	G-A	DLOOP2	98	1	non-coding
189	PK_83	BE	A-G	DLOOP2	3	1	non-coding
195	PK_28	BE	T-C	DLOOP2	15	1	non-coding
237	PK_94	BE	A-G	DLOOP2	3	1	non-coding
279	PK_75	BE	T-G	DLOOP2	2	0	non-coding
877	PK_68	BE	G-A	RNR1	8	0	non-coding
2170	PK_82	BE	G-A	RNR2	3	0	non-coding
2582	PK_74	BE	A-G	RNR2	3	0	non-coding
2943	PK_30	BE	G-A	RNR2	2	0	non-coding
3469	PK_34	BE	C-T	ND1	5	0	L55F
3907	PK_30	BE	G-A	ND1	23	0	A201T
4058	PK_53	BE	C-T	ND1	4	0	S251F
4380	PK_99	BE	C-T	TQ	4	0	syn
6269	PK_34	BE	A-G	CO1	3	0	syn
6293	PK_82	BE	T-C	CO1	10	1	syn
6729	PK_28	BE	G-A	CO1	3	0	A276T
7765	PK_96	BE	A-G	CO2	4	1	syn
8093	PK_30	BE	T-C	CO2	6	1	syn
9406	PK_83	BE	A-G	CO3	4	0	Y67C
10551	PK_97	BE	T-C	ND4L	59	0	S28P
11274	PK_99	BE	G-A	ND4	15	0	G172D
12131	PK_32	BE	T-C	ND4	85	0	S458P
12979	PK_87	BE	G-A	ND5	2	0	G215S
14569	PK_68	BE	G-A	ND6	3	1	syn
15466	PK_81	BE	G-A	CYB	3	1	syn
15642	PK_97	BE	T-C	CYB	70	0	L299P
15777	PK_68	BE	G-A	CYB	4	1	S344N
15995	PK_30	BE	G-A	TP	15	0	non-coding
16335	PK_67	BE	A-G	DLOOP1	97	1	non-coding
16519	PK_94	BE	T-C	DLOOP1	94	0	non-coding

Heteroplasmies found only in malignant tissue samples (private cancer heteroplasmies)							
153	PK_46	CA	A-G	DLOOP2	75	1	non-coding
153	PK_89	CA	A-G	DLOOP2	98	1	non-coding
195	PK_72	CA	T-C	DLOOP2	98	1	non-coding
204	PK_80	CA	T-C	DLOOP2	4	1	non-coding
215	PK_99	CA	A-G	DLOOP2	3	1	non-coding
228	PK_47	CA	G-A	DLOOP2	6	1	non-coding
295	PK_57	CA	C-T	DLOOP2	2	1	non-coding
605	PK_98	CA	T-C	TF	18	0	non-coding
879	PK_34	CA	T-C	RNR1	7	0	non-coding
1062	PK_97	CA	G-A	RNR1	5	0	non-coding
1454	PK_46	CA	G-A	RNR1	43	0	non-coding
1538	PK_54	CA	G-A	RNR1	2	0	non-coding
1896	PK_74	CA	T-C	RNR2	39	0	non-coding
1949	PK_46	CA	G-A	RNR2	4	0	non-coding
2009	PK_35	CA	G-A	RNR2	3	0	non-coding
2022	PK_80	CA	G-A	RNR2	5	0	non-coding
2174	PK_40	CA	G-A	RNR2	3	0	non-coding
2643	PK_32	CA	G-A	RNR2	5	0	non-coding
2667	PK_89	CA	T-C	RNR2	8	0	non-coding
2702	PK_66	CA	G-A	RNR2	6	1	non-coding
2702	PK_98	CA	G-A	RNR2	11	1	non-coding
2777	PK_97	CA	G-A	RNR2	3	0	non-coding
2833	PK_83	CA	A-G	RNR2	11	1	non-coding
3070	PK_83	CA	G-A	RNR2	15	0	non-coding
3127	PK_46	CA	G-A	RNR2	4	0	non-coding
3226	PK_46	CA	G-A	RNR2	60	0	non-coding
3421	PK_35	CA	G-A	ND1	7	1	V39I
3850	PK_79	CA	G-A	ND1	2	0	A182T
4036	PK_87	CA	G-A	ND1	5	0	syn
4142	PK_49	CA	G-A	ND1	11	0	R279Q
4209	PK_54	CA	T-C	ND1	7	1	syn
4522	PK_98	CA	T-C	ND2	19	0	L18P
4665	PK_53	CA	G-A	ND2	6	0	A66T
4853	PK_67	CA	G-A	ND2	5	1	syn
4896	PK_54	CA	T-C	ND2	17	1	Y143H
5359	PK_44	CA	T-C	ND2	30	0	I297T
5539	PK_62	CA	A-G	TW	12	1	syn
5920	PK_96	CA	G-A	CO1	56	0	syn
6027	PK_40	CA	G-A	CO1	2	0	G42S
6186	PK_53	CA	C-T	CO1	18	0	P95S
6321	PK_34	CA	G-A	CO1	56	0	syn
6329	PK_34	CA	C-T	CO1	2	0	syn
6579	PK_50	CA	G-A	CO1	4	0	syn
6844	PK_89	CA	T-C	CO1	79	0	I314T
7084	PK_40	CA	T-C	CO1	4	0	I394T

7589	PK_65	CA	G-A	CO2	2	0	A2T
7702	PK_44	CA	G-A	CO2	6	1	syn
7854	PK_79	CA	T-C	CO2	5	0	V90A
7886	PK_42	CA	G-A	CO2	90	0	G101S
7910	PK_73	CA	G-A	CO2	3	0	E109K
7986	PK_50	CA	G-A	CO2	8	0	R134Q
8921	PK_77	CA	G-A	ATP6	4	0	G132D
9010	PK_80	CA	G-A	ATP6	5	1	A162T
9379	PK_54	CA	G-A	CO3	23	0	syn
9386	PK_89	CA	T-C	CO3	4	1	syn
9460	PK_28	CA	T-C	CO3	44	0	L85P
9658	PK_87	CA	T-C	CO3	65	0	L151P
9837	PK_75	CA	G-A	CO3	5	0	G211S
9893	PK_65	CA	C-T	CO3	7	0	syn
10326	PK_34	CA	T-C	ND3	38	0	S90P
10353	PK_81	CA	G-A	ND3	60	0	A99T
10731	PK_62	CA	G-A	ND4L	6	0	D88N
10773	PK_53	CA	T-C	ND4	13	0	I5T
11195	PK_33	CA	G-A	ND4	3	0	G146S
11891	PK_79	CA	G-C	ND4	4	0	E378Q
11991	PK_96	CA	T-C	ND4	82	0	F411S
12805	PK_95	CA	T-C	ND5	55	0	W157R
13115	PK_40	CA	T-C	ND5	9	0	L260P
13288	PK_54	CA	G-A	ND5	3	0	G318S
13495	PK_63	CA	A-G	ND5	81	0	T387A
13886	PK_80	CA	T-C	ND5	5	1	L517P
13915	PK_28	CA	G-A	ND5	62	0	syn
13915	PK_33	CA	G-A	ND5	9	0	syn
13916	PK_44	CA	G-A	ND5	3	0	G527E
14663	PK_66	CA	G-A	ND6	39	0	A4V
15388	PK_49	CA	T-C	CYB	9	1	syn
15479	PK_53	CA	T-C	CYB	7	1	F245L
15617	PK_30	CA	G-A	CYB	3	1	V291I
15719	PK_65	CA	T-C	CYB	9	1	Y325H
16093	PK_49	CA	T-C	DLOOP1	74	1	non-coding
16108	PK_96	CA	C-T	DLOOP1	16	1	non-coding
16129	PK_83	CA	G-A	DLOOP1	21	1	non-coding
16266	PK_96	CA	C-T	DLOOP1	9	1	non-coding
16519	PK_89	CA	T-C	DLOOP1	15	0	non-coding

Table S4: Logistic regression analysis.

A. Analysis including all mtDNA Heteroplasmies (non-coding, synonymous and non-synonymous). Age [a], free serum PSA ratios [%] and tumor stage (pT) were independent variables. Variables that did not show a correlation with the presence of mtDNA heteroplasmies in univariate analysis were not included. **B.** Analysis on non-synonymous heteroplasmies in PCa samples only. High-grade staging (Gleason score>7), age [a] and free serum PSA ratios [%] were independent variables. Variables that did not show a correlation with the presence of non-synonymous mtDNA heteroplasmies in the malignant tissue in univariate analysis were not included. Variable coefficients, standard errors (S.E.), odds ratios (O.R.) including their 95% confidence intervals (Ci) and *p*-values (*p*).

Variable	Coefficient	S.E.	*p*	O.R. (95% Ci)
A. All heteroplasmies				
age at diagnosis [a]	0.089	0.043	0.040	1.093 (1.004 - 1.189)
free PSA [%]	-0.118	0.060	0.048	0.889 (0.790 - 0.999)
pT stage	-0.916	0.538	0.088	0.400 0.139 - 1.147)
B. Non-synonymous heteroplasmies in PCa tissue only				
Gleason score >7	2.170	0.958	0.022	8.759 (1.340 – 57.26)
age at diagnosis [a]	-0.084	0.046	0.068	0.920 (0.841 - 1.006)
free PSA [%]	-0.133	0.067	0.045	0.875 (0.768 – 0.997)

TableS5. Tissue samples for RNA Seq (*N*=16)

Tumor cases were chosen for mRNA expression analyses based on the relative contribution of GM-pathway OXPHOS capacity (GM_P) to PGMS-OXPHOS capacity. In addition, Gleason-scores were considered. Low GM-pathway capacity, representing a severe respiratory phenotype, was defined as ≤0.27 while high GM-pathway capacity, representing a mild respiratory phenotype, was defined as >0.27, respectively.

Sample ID	Gleason score	Relative GM-pathway capacity
PK 28	7	high (0.30)
PK 31	7	high (0.57)
PK 34	7	high (0.37)
PK 41	7	high (0.29)
PK 44	7	low (0.27)
PK 46	9	high (0.30)
PK 47	6	low (0.13)
PK 50	9	low (0.22)
PK 54	9	low (0.12)
PK 60	9	low (0.14)
PK 62	7	low (0.17)
PK 65	7	high (0.31)
PK 72	7	high (0.34)
PK 80	7	low (0.27)
PK 82	10	low (0.12)
PK 90	6	high (0.28)

Supplementary figures

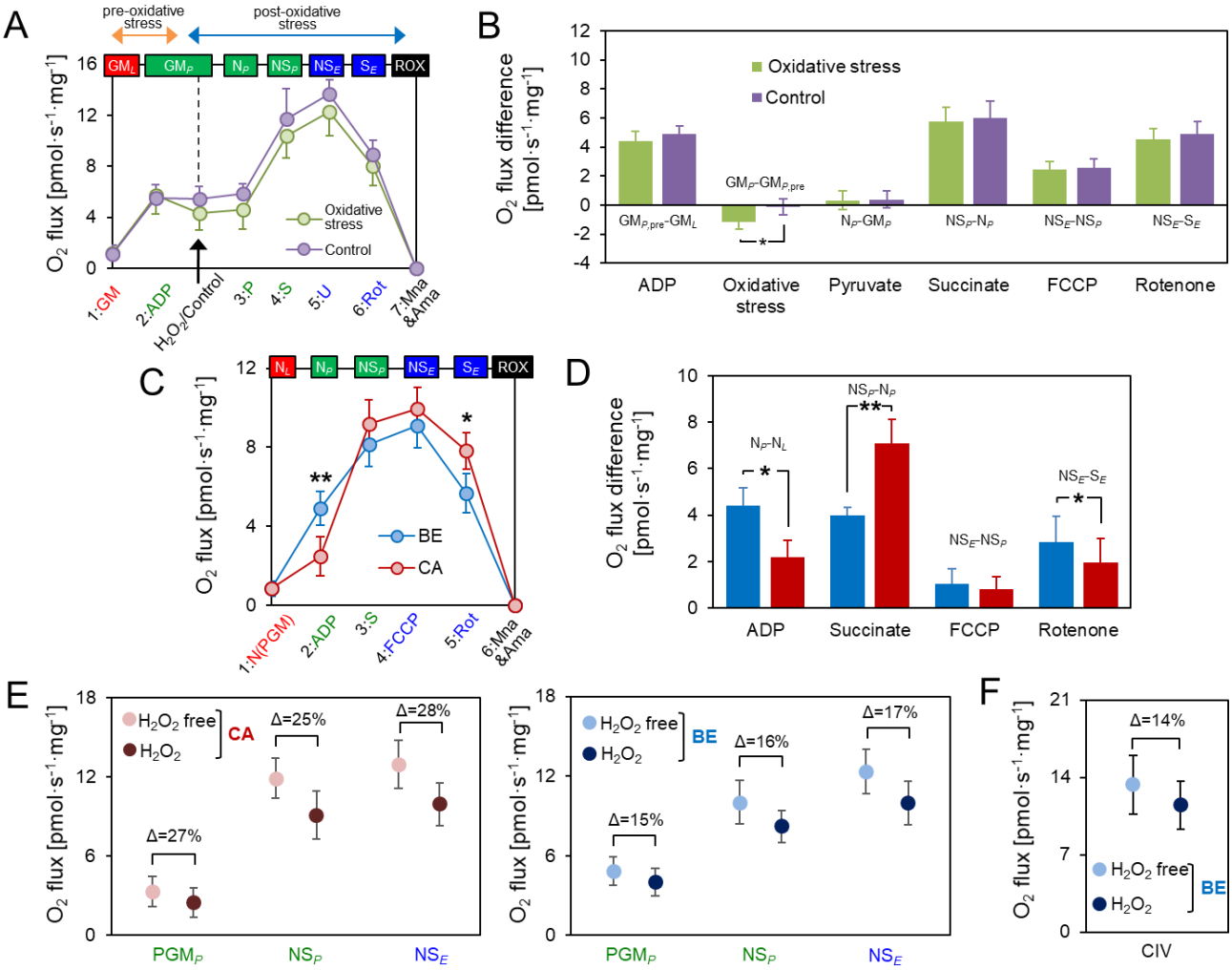

Supplementary Fig. S1. Effect of oxidative stress by H_2O_2 incubation on respiratory capacities. A. Oxidative stress test by 15 min exposure to 500 µM H_2O_2 or H_2O as control: O_2 flux in split BE tissue samples (*N*=6). The arrow indicates the titration of H_2O_2 or H_2O into the O2k chamber. **B**. Effects of substrates glutamate&malate (ADP), pyruvate, succinate, H_2O_2 or H_2O, uncoupler FCCP, and CI inhibitor rontenone on O_2-flux in split tissue samples subjected to a SUIT protocol with (green) or without (pink) oxidative stress treatment. **C-D.** HRR analysis in paired BE/CA tissue samples (*N*=6) applying a SUIT protocol without oxidative stress treatment. **C.** O_2-flux in the indicated coupling/pathway control states in benign (blue) and malignant (red) tissue samples. **D.** Effect of substrates, uncoupler and CI-inhibitor rotenone on O_2-flux in the benign (blue) and malignant (red) tissue samples. **E.** Comparison of respiratory capacities in the indicated coupling/pathway control states in paired benign (blue) and tumor red) samples analyzed without imposed oxidative stress (*N*=6, light colors) compared to paired samples analyzed with inclusion of the oxidative stress step (*N*=50, dark colors). **F.** Effect of oxidative stress by H_2O_2 treatment on CIV activity. O_2-flux was measured in split benign samples (*N*=6) after treatment with 500 µM H_2O_2 to mimic oxidative stress (dark blue) or H_2O (light blue) as control. Values represent mean ± SD. See legend to Fig. 2 and Tables S1 and S2 for description of the respiratory states.

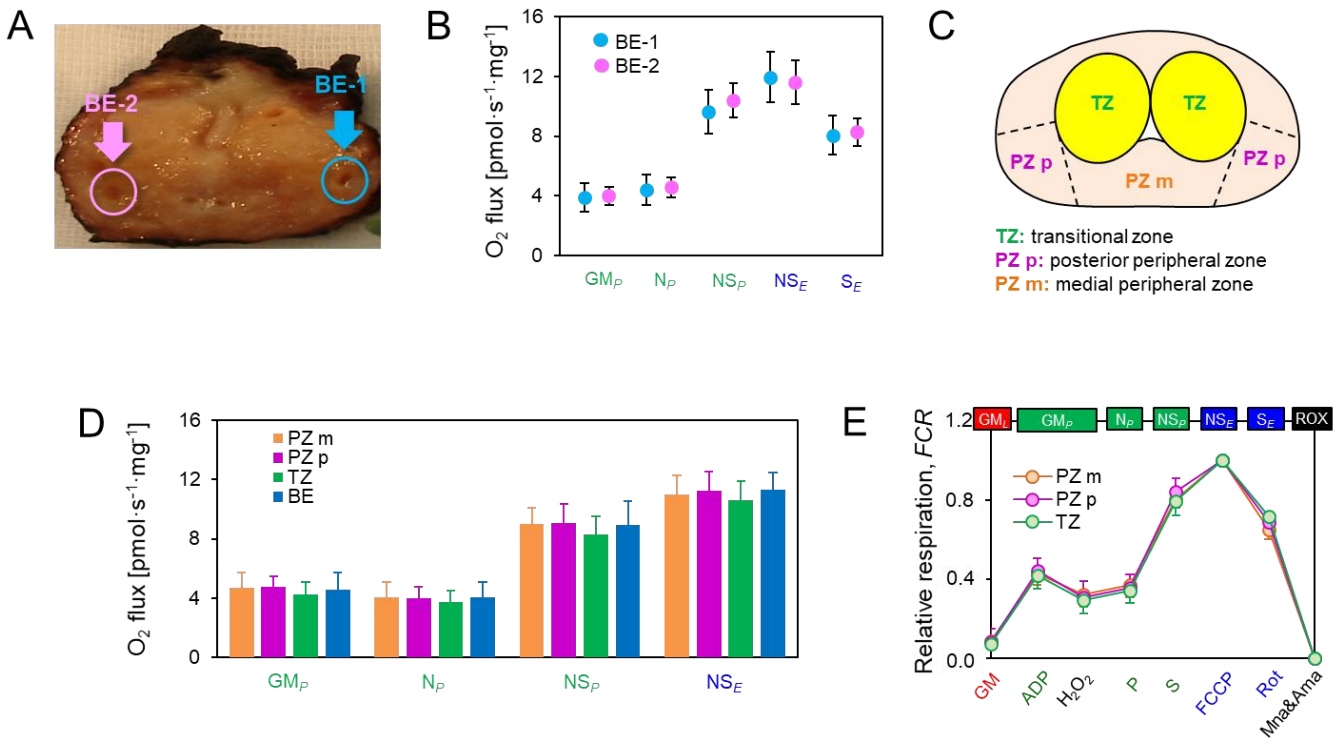

Supplementary Fig. S2. OXPHOS capacities in paired benign tissue obtained from different locations in the gland. A. Paired benign tissue samples (BE-1 and BE-2) from 20 radical prostatectomy specimens were extracted distant from each other, normally from the contralateral site, via punch needle biopsy by a certified uropathologist. Benign status was confirmed by histopathology analysis as shown in Fig. 1. **B.** Comparison of OXPHOS- and ET-capacities of indicated states in paired BE/BE tissue samples. The same SUIT protocol as for BE/CA paired sample analysis was applied. **C.** Schematic representation of a prostate cross-section and the zonal architecture. Tissue biopsies for the pairwise comparison of BE-1 and BE-2 samples were obtained from the transitional zone (TZ) or medial or posterior peripheral zone (PZ m and PZ p, respectively). **D.** Comparison of OXPHOS- and ET-capacities in benign samples (BE-1 and BE-2) extracted from the PZ m (orange; *N*=17), the PZ m (magenta; *N*=18), the TZ (green; *N*=5) and in the BE samples from the paired BE/CA analysis (blue; *N*=50). **F.** Normalized respiratory capacities in benign samples (BE-1 and BE-2) extracted from the PZ m (orange; *N*=17), the PZ m (magenta; *N*=18), the TZ (green; *N*=5). All values represent mean ± SD. See legend to Fig. 2 and Tables S1 and S2 for description of the respiratory states.

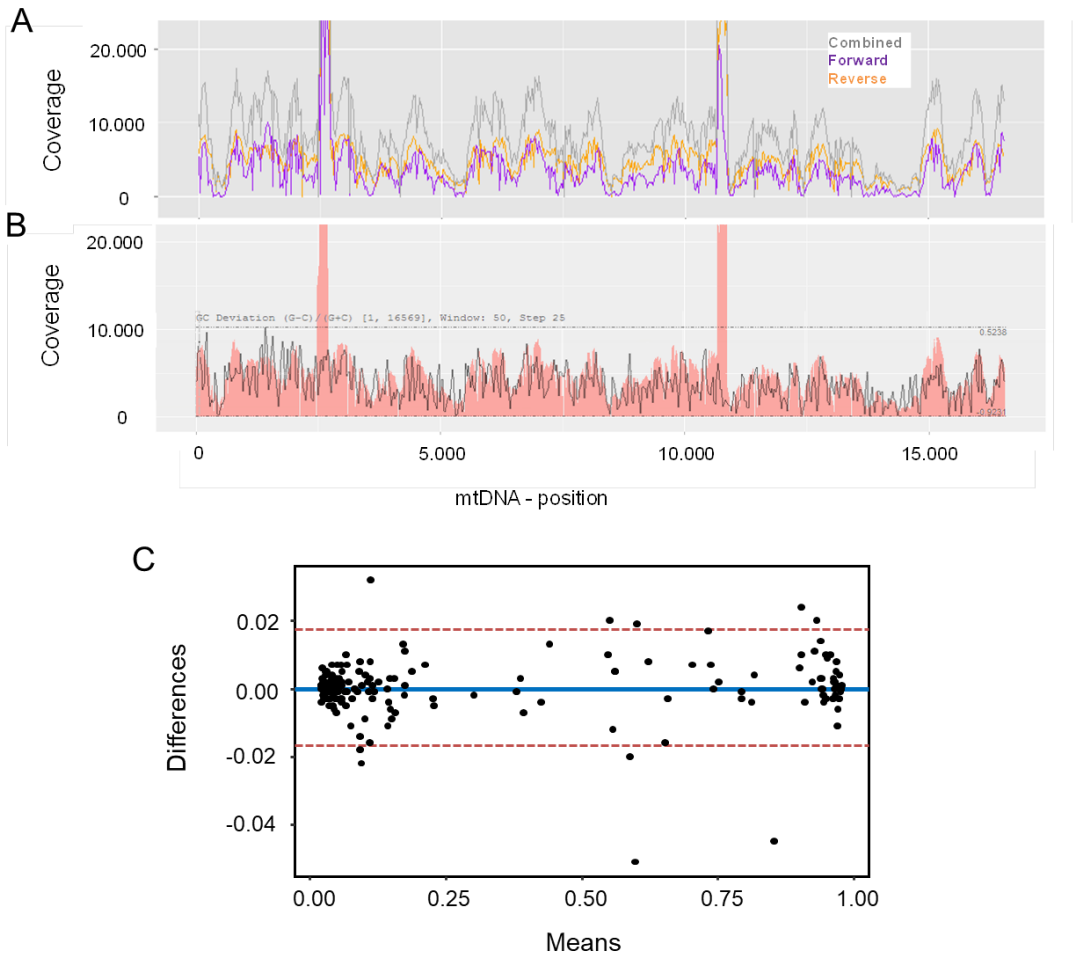

Supplementary Fig. S3. Mean forward and reverse mtDNA nucleotide coverage, mtDNA coverage correlated to GC content and Bland-Altmann plot of all variants as detected by two independent sequencing runs. A. Coverage of forward (purple), reverse (orange) as well as the combined coverage (grey) along the mtDNA of an Ion Proton sequencing run of 40 barcoded samples. The two high coverage peaks represent the overlapping areas of the two long-range PCR amplicons covering the entire mt-genome. **B.** Influence of GC content. The mean nucleotide coverage of the reverse reads (orange) is highly concordant with the GC content (grey line) of the DNA sequence. This pattern was seen for all samples and all sequencing runs, irrespective of library concentration used for ISP generation, Chip loading density or nucleotide coverage. **C.** Bland-Altmann plot of the concordance between the two runs. Values on the *x*-axis represent the mean heteroplasmy level while values on the *y*-axis represent the minor allele frequency (MAF) differences between the two runs for each variant.

A

Sample	Locus	Variant	RNA alteration	HP level	MitoTIP prediction
PK_30	MT-TP	G15995A	U	15%	likely pathogenic
PK_62	MT-TW	A5539G	C	12%	likely benign
PK_98	MT-TF	T605C	G	18%	Not reported
PK_99	MT-TQ	C4380T	A	4%	likely benign

B

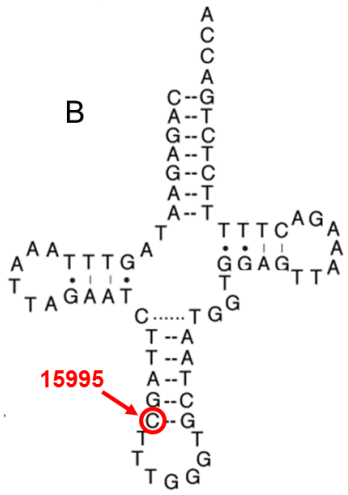

Supplementary Fig. S4. MT-tRNA mutations in benign and malignant tissue samples detected via NGS. A. List of samples harboring mtDNA encoded tRNA mutations. Listed are the location (MT-TP= $tRNA^{Pro}$, MT-TW= $tRNA^{Trp}$, MT-TF= $tRNA^{Phe}$, MT-TQ= $tRNA^{Glx}$), the variant, the alteration of RNA sequence caused by the variant, the HP level of the variant and the predicted pathogenic effect as determined by MitoTIP (https://www.mitomap.org/cgi-bin/mitotip). **B.** Cloverleaf structure of mtDNA encoded $tRNA^{Pro}$. The red circle indicates the location on the anticodon stem affected by the G>A substitution at position 15995. This mutation most likely leads to a destabilization in RNA folding since it is the last base pair required for the stabilization of the anticodon loop.

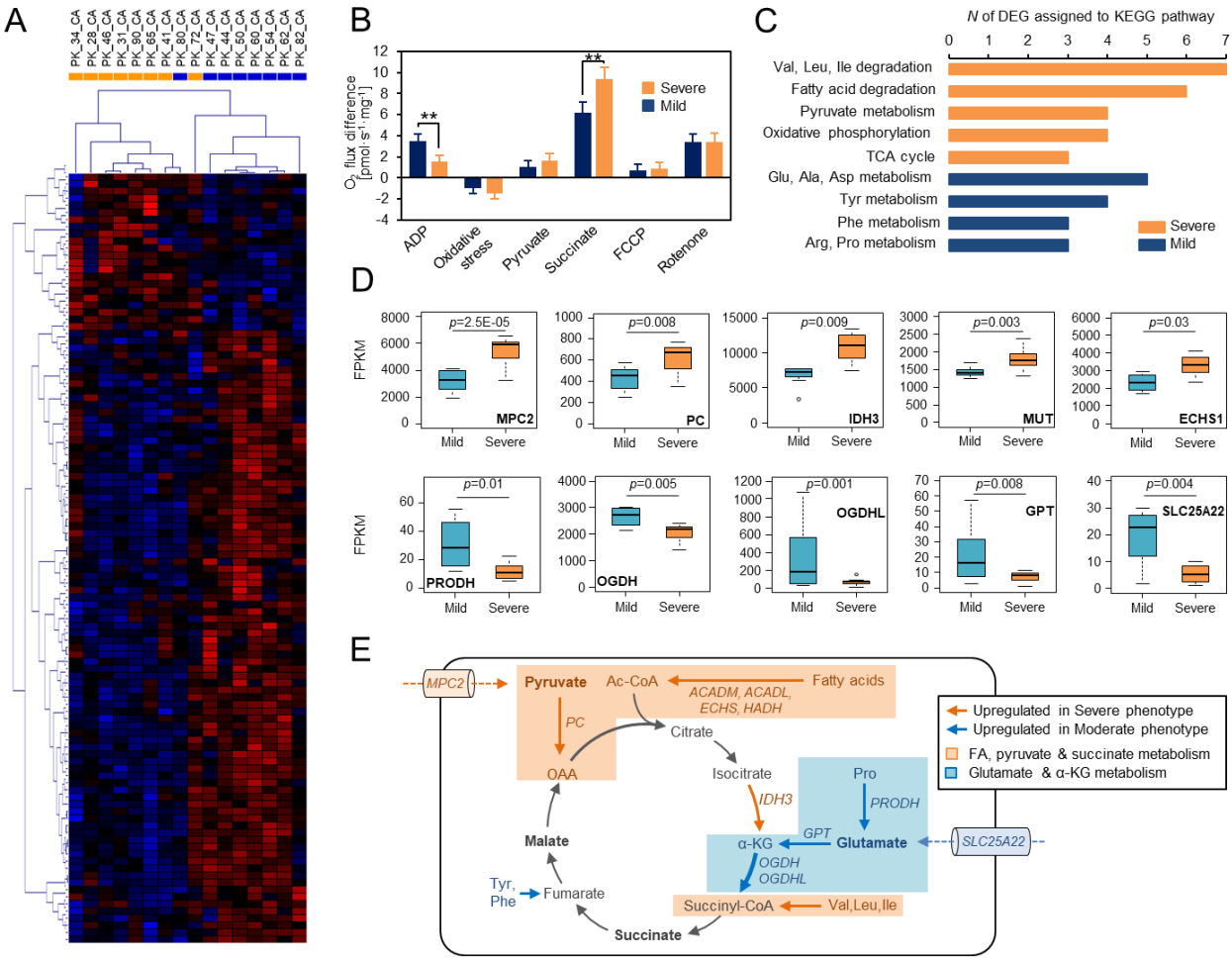

Supplementary Fig. S5. Differential mRNA expression of mitochondrial genes and enriched metabolic KEGG pathways in malignant samples exhibiting a severe or mild respiratory phenotype. A. Heatmap and hierarchical clustering of all significantly differentially expressed mitochondria-related genes (*FDR*<0.1) based on the MitoCarta2.0 Gene Catalog in the severe (orange) or mild (light blue) respiratory phenotype tumor samples. **B.** Effects of substrates glutamate&malate (ADP), pyruvate, succinate, oxidative stress, uncoupler FCCP, and CI inhibitor rontenone on O_2-flux in tissue samples used for transcriptome profiling by RNA-seq. Tumor samples obtained from 16 radical prostatectomies were grouped according to their respiratory phenotype in a mild phenotype (blue) and severe phenotype (orange) group, respectively (Table S5). **C.** Enriched metabolic KEGG pathways upregulated (red) or downregulated (blue) in cancer tissue based on the InnateDB pathway over-representation analysis of all differentially expressed mt-related genes. **D.** Boxplot representing fragments Per Kilobase Million (FPKM) values for expression of significantly differently expressed metabolic key-enzymes in tumor samples exhibiting a severe (orange) or mild (light blue) respiratory phenotype (MPC2: mitochondrial pyruvate carrier 2; PC: pyruvate carboxylase; IDH3: isocitrate dehydrogenase 3 subunit gamma; MUT: methylmalonyl-CoA mutase; ECHS1: enoyl-CoA hydratase, short chain 1; PRODH: proline dehydrogenase; GPT: glutamate-pyruvate transaminase; OGDH: 2-oxoglutarate/α-ketoglutarate dehydrogenase; OGDHL: 2-oxoglutarate/α-ketoglutarate dehydrogenase dehydrogenase like; SLC25A22: solute carrier family 25 member 22=mitochondrial glutamate carrier). **E.** Detailed annotation of single up-regulated TCA-cycle key-enzymes in the severe (orange) or mild (light blue) respiratory phenotype samples. Blue boxes mark steps mainly involved in glutamate- and α-ketoglutarate-linked electron transfer and orange boxes highlight steps related to fatty acid, pyruvate and succinate mediated electron transfer. Substrates used in HRR analysis (malate, glutamate, pyruvate, and succinate) are indicated in bold type while orange and light blue colored names and arrows mark enzymes and enzymatic reactions that are upregulated in samples exhibiting either a severe or mild respiratory phenotype, respectively.